Generation, Characterization and Application of the 3rd and 4th Harmonics of a Ti:sapphire Femtosecond Laser

by

Peter C. Wright

Thesis submitted to the

Faculty of Graduate and Postdoctoral Studies

In partial fulfillment of the requirements

For the M.Sc. degree in

Physics

Sciences

University of Ottawa

© Peter C. Wright, Ottawa, Canada, 2012

Abstract

Femtosecond time-resolved photoelectron spectroscopy (fsTRPES) experiments have been used to study the photoelectron energy spectra of simple molecules since the 1980's. Analysis of these spectra provides information about the ultrafast internal conversion dynamics of the parent ions. However, ultraviolet pulses must be used for these pump-probe experiments in order to ionize the molecules. Since current solid state lasers, such as the Ti:sapphire laser, typically produce pulses centered at 800nm, it is necessary to generate UV pulses with nonlinear frequency mixing techniques. I therefore constructed an optical setup to generate the 3rd and 4th harmonics, at 266.7nm and 200nm, respectively, of a Ti:sapphire (Ti:sa) chirped-pulse amplified (CPA) laser system that produces 35fs pulses centered at 800nm. Thin Beta-Barium Borate (β-BaB_2O_4 or BBO) crystals were chosen to achieve a compromise between short pulse durations and reasonable conversion efficiencies, since ultrashort pulses are quite susceptible to broadening from group velocity dispersion (GVD).

Output energies of around 11μJ and 230nJ were measured for the 266.7nm and 200nm pulses, respectively. The transform limits of the 3rd and 4th harmonic pulse lengths were calculated from their measured spectral widths. We found that the 266.7nm bandwidth was large enough to support sub-30fs pulses, and due to cutting at the lower-wavelength end of the 200nm spectrum, we calculated an upper limit of 38fs. The pulses were compressed with pairs of CaF_2 prisms to compensate for dispersion introduced by transmissive optics. Two-photon absorption (TPA) intensity autocorrelations revealed fully compressed pulse lengths of 36 ± 2 fs and 42 ± 4 fs for the 3rd and 4th harmonics, respectively.

Acknowledgements

I would first and foremost like to thank my research supervisor, Dr. Albert Stolow, for his guidance and support throughout my graduate work. His expertise and encouragement helped me to overcome roadblocks along the way, and improved my confidence and ability as a researcher.

I would also like to thank the other graduate students and postdoctoral fellows in my research group, especially Drs. Rune Lausten, Iain Wilkinson, Jochen Mikosch and Paul Hockett, as well as Owen Clarkin, who were all of invaluable help throughout my project. I greatly appreciate all of their patience and encouragement throughout my master's, as well as a few late nights spent working in the lab.

I would also like to thank Denis Guay and Doug Moffatt for all of their assistance in the machine shop, as well as with the wiring and assembly of the necessary electronics and the implementation of the Labview code for the TPA intensity autocorrelation measurements.

Most importantly, I would like to thank my parents as well as the rest of my family and friends for all of their love and support, especially over the past two years. They have stood by me and helped me through all of the obstacles that I encountered along the way, and I would not have been able to do this without them. And lastly, a special thank you to Katrina for keeping me sane throughout the final few months of my thesis.

Table of Contents

List of Tables

List of Figures

Chapter 1: Introduction to Ultrashort Laser Pulses and Harmonic Generation

1.1 – Advancements in Laser Technology

Prior to the development of the first working laser in 1960 by Theodore Maiman [1], it was only possible to study linear optical processes, which, as the name suggests, scale linearly with the intensity of light. However, such limitations were overcome with the advent of this coherent, monochromatic source of radiation, whose inherently large intensities opened the door to the study of nonlinear optical (NLO) processes. Many researchers quickly developed new types of lasers that same year, such as the He-Ne laser [2], improving on Maiman's initial design, which used Ruby as the gain medium. Early experimental observations of NLO processes such as two-photon excitation [3], second harmonic generation (SHG) [4] and sum-frequency generation (SFG) [5], all of which will be discussed in subsequent chapters, resulted in the rapid growth of NLO as an important area of scientific research.

An important step in laser technology was the ability to produce a pulsed output. Early laser pulse generation was achieved with Q-switching [6], which uses an electro-optic modulator, such as a Kerr cell [6], to generate pulses of much greater intensity than the previous continuous-wave (CW) output. When a voltage is applied to the Kerr cell, which is placed between the gain medium and one of the end mirrors of the laser cavity, it behaves as a waveplate, rotating the polarization of the incident electric field by an amount dependent on its orientation [6]. Since the cavity end mirrors are more reflective for a particular polarization, the quality factor, or Q factor, which describes the attenuation of light inside of the cavity due to resonator losses, can be controlled with the Kerr cell.

By adjusting the polarization such that the cavity losses are high, corresponding to a low Q factor, the gain in the light, and hence population inversion leading to lasing, will be suppressed. Thus, the energy builds up inside of the cavity until the Kerr cell is turned off, at which point the light returns to its original polarization, causing the Q factor to switch from low to high, releasing the energy in the cavity in the form of a short, intense, optical pulse [6]. The typical pulse durations of early Q-switched lasers were on the order of several 10's of nanoseconds, the first pulses being around 120 ns in duration [6].

Pulses in the picosecond domain were achieved with the development of mode-locking [7], which has remained the standard method of laser pulse generation. This technique produces pulses by locking the laser cavity's longitudinal modes in phase so that once every cavity round trip, they constructively interfere to generate a pulse shorter and more intense than with Q-switching alone. Mode-locking can be achieved by modulating the losses in the cavity at the frequency of the cavity mode spacing. For a laser cavity of length L, the modes are equally spaced, corresponding to a free spectral range (FSR) of [8]

$$\Delta\nu = \frac{c}{2L} \tag{1.1.1}$$

where c is the speed of light. Figure 1.1 illustrates the resulting power spectrum typical of a mode-locked laser.

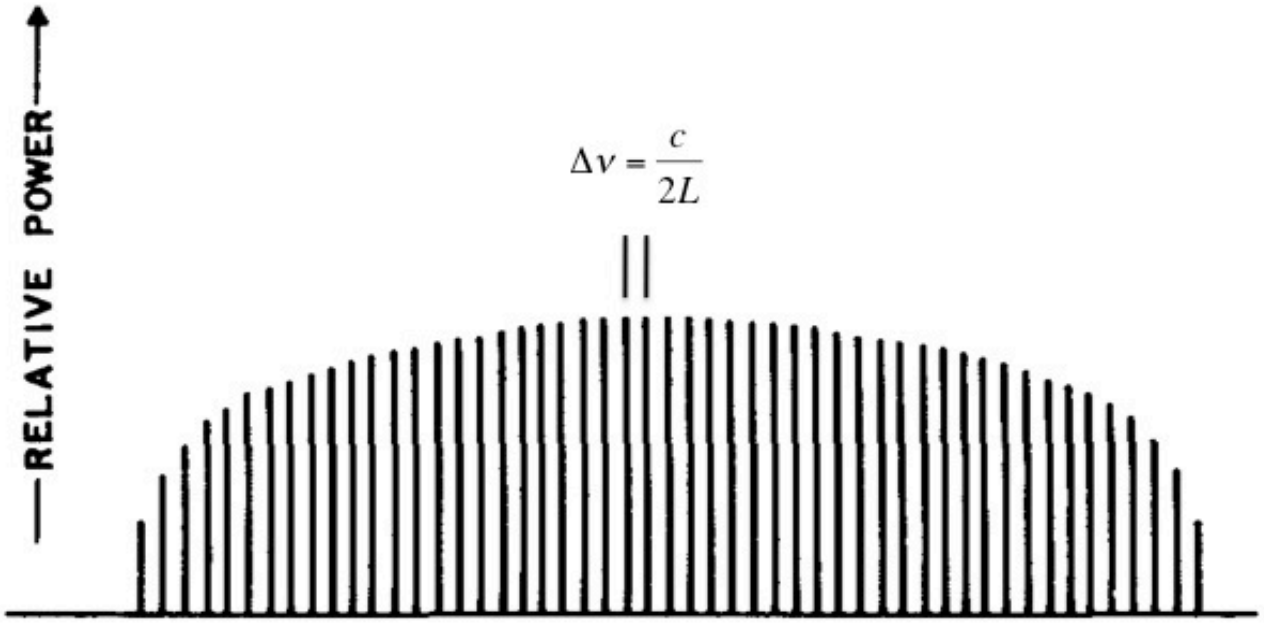

Fig. 1.1 – Reproduction of the power spectrum of a mode-locked Nd:YAG laser measured by DiDomenico *et al*. [8]. The horizontal axis represents the mode frequencies, which are equally spaced according to (1.1.1).

As explained by DiDomenico *et al*. [8], the pulse duration and energy are controlled by the bandwidth of the gain medium, as it is the bandwidth that dictates the number of modes oscillating inside the laser cavity. Therefore, the larger the gain bandwidth, the shorter and more energetic the pulses, as seen in initial studies using Neodymium-doped yttrium aluminium garnet (Nd:$Y_3Al_5O_{12}$, or Nd:YAG) as the gain medium in a mode-locked laser that produced pulses on the order of 150 ps [8].

Even shorter pulse durations were achieved with a passive mode-locking technique using a saturable absorber, such as a reversible bleachable dye, as the modulating element. Instead of being externally driven, or "actively" mode-locked, the saturable absorber responds to the intensity of the incident light inside of the laser cavity and selectively transmits larger intensities while attenuating lower ones [9]. This technique allows for the transmission of the highest pulse amplitudes, while reducing noise and reflections as well as producing shorter pulse lengths [10, 11, 12]. The sub-100 femtosecond time domain of

ultrashort pulses was breached by Fork *et al*. in 1981, using a novel technique in conjunction with passive mode-locking, known as "colliding pulse mode-locking", to achieve pulse durations of 90 fs [13].

As we will see, ultrashort pulse durations are extremely important for numerous applications. Equally important, however, is the ability to produce a broad range of wavelengths, since many applications require different photon energies. As such, the use of solid state gain media, such as Ti:sapphire (Ti:sa) [14], was a key development in tunable laser technology. Ti:sa lasers have a broadly tunable spectrum between roughly 680 – 1100nm, centered at 800nm [15, 16]. This particular wavelength range is well suited for nonlinear mixing techniques, which can produce light deep into the UV or further into the IR depending on the desired application.

In addition to its spectrum being broader than that of most dye lasers, Ti:sa, along with other solid state gain media, has a higher saturation fluence, or threshold, allowing for the generation of pulses of much higher energy [16]. Normally, the ultrashort pulses produced by these lasers would be limited to energies below the damage threshold of the Ti:sa crystal. However, through a technique known as "chirped pulse amplification" (CPA) [17], the full saturation fluence of the Ti:sa can be exploited to produce pulses with very large energies, while avoiding any damage to the gain medium as well as unwanted nonlinear optical phenomena. With CPA, short pulses produced by an oscillator are stretched using, for example, a grating pair, producing long ps pulses with low energies. These pulses are then amplified, typically either with a regenerative amplifier or multipass amplifier [16, 18], or both, to the mJ range.

A regenerative amplifier uses an electro-optic modulator, such as a Kerr or Pockels cell, to trap the stretched pulses inside of a laser cavity containing a gain medium, such as a

Ti:sa crystal [16]. The pulses then circulate inside of the cavity, increasing in energy with each pass through the crystal, until the electric field supplied to the electro-optic modulator is turned off, allowing the amplified pulses to exit the cavity. Pulses typically make between 10 and 15 passes through the gain medium in regenerative amplifiers, although this number is adjustable depending on the desired amplification [16]. A multipass amplifier, on the other hand, achieves amplification with a series of mirrors that send the pulses through the gain medium (ie. Ti:sa crystal) at offset angles. The number of passes through the gain medium is typically fewer than 10, allowing for it to be pumped harder than for the regenerative amplifier [16, 18]. Multipass amplifiers are therefore well suited to producing pulses of even greater energies than those achieved with regenerative amplifiers, and these two amplification systems are often used in succession [16].

After amplification, the pulses are compressed back to their initial transform limited durations, resulting in ultrashort pulses with extremely large energies and peak powers that are well suited to NLO studies [16]. For these reasons, mode-locked Ti:sa CPA laser systems have become commercial standards in many labs today, including the femtosecond labs at the Steacie institute for molecular sciences (SIMS) at the National Research Council of Canada (NRC), where the work presented in this thesis was performed.

1.2 – Applications of Ultrashort Laser Pulses

The short durations, high peak powers and broad spectral bandwidths of ultrashort laser pulses are unique properties that make them quite useful for numerous applications such as laser micromachining [19, 20, 21], ophthalmology [19] and broadband optical communication [19, 22]. Furthermore, femtosecond pulses have greatly advanced many

areas of nonlinear microscopy, such as Coherent anti-Stokes Raman Scattering (CARS) microscopy. This technique allows for the imaging of live biological samples by using nonlinear frequency mixing to produce non-resonant, coherent radiation that is sensitive to the vibrations of different chemical species or cellular components [23, 24].

The above examples are just a few of the myriad of applications of femtosecond lasers. However, one of the earliest and most fundamental applications of ultrashort laser pulses is to the field of time-resolved studies of ultrafast processes, notably molecular dynamics. With the advancement of laser technology pushing tunable pulses to much shorter durations, higher peak powers and greater stability, the field of ultrafast molecular dynamics continues to grow as an exciting area of modern research. This topic, specifically that of time-resolved photoelectron spectroscopy (TRPES), is one of the primary subjects of research in the SIMS molecular photonics group.

1.3 – Time-Resolved Photoelectron Spectroscopy (TRPES)

When excited by a laser pulse, a polyatomic molecule will undergo a mixing of vibrational and electronic motions, which result in charge redistribution and energy flow within the molecule [25]. These chemical reactions occur within 10's to a few hundred femtoseconds, making modern fs laser systems excellent tools for monitoring the reactions in real time as they progress from reactants to transition states to products [26]. Ultrafast molecular dynamics are of course important for our fundamental understanding of chemistry, but they also play an essential role in many biological processes such as vision [25, 27].

TRPES thus refers to the study of molecular dynamics through the analysis of the photoelectron spectra obtained with femtosecond temporal resolution. The primary

experimental method for observing molecular dynamics is known as pump-probe spectroscopy, whereby an initial pump pulse is used to excite the molecule, forming a superposition of vibrational states referred to as a wavepacket. Upon excitation, the molecule will undergo a dynamic transition to the final state via evolution of the vibronic and electronic states, known as internal conversion [25]. A secondary probe pulse of higher energy then arrives at the molecule after some time delay, mapping the dynamics onto the final state, which is typically achieved via photoionization. The ionization process is a useful way to study molecular dynamics because the differential technique of photoelectron detection is simple and allows for the distinction to be made between different frequency components of the wavepacket [28]. This allows for further analysis of the photoelectron kinetic energy distribution, which provides details of the internal conversion dynamics [28].

For example, TRPES measurements performed by Blanchet *et al*. on a linear unsaturated hydrocarbon chain (DT, $C_{10}H_{14}$) [25] showed that internal conversion of vibrational states led to an evolving electronic state, which was seen as a switching of the photoelectron band in the photoelectron kinetic energy spectrum [25].

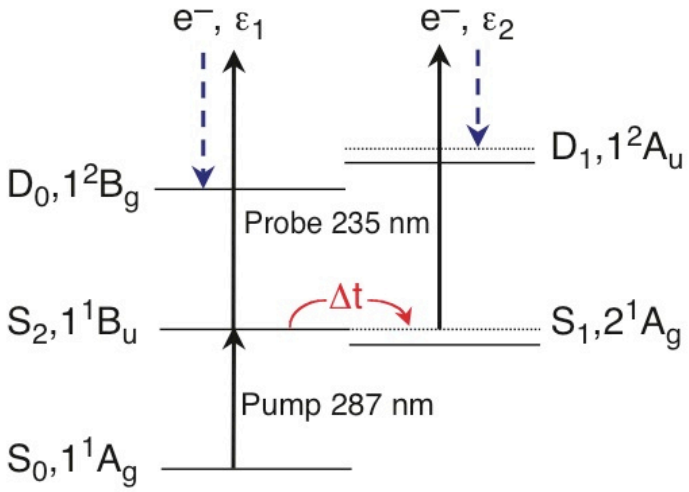

Fig. 1.2 – The electronic level scheme in $C_{10}H_{14}$ for one-photon probe ionization. Due to ultrafast internal conversion, switching of the photoelectron band occurs. The dashed blue lines indicate electron emission [25].

When initially excited to the state S_2, the molecule would occupy the D_0 ion state upon ionization. However, the measured photoelectron energy spectrum showed that after 386 fs, subsequent photoionization resulted in the occupation of the D_1 ion state. This is attributed to the evolution of the molecule to an optically forbidden state, S_1, due to internal conversion, in which D_1 is the only accessible ion state [25].

Pump-probe experiments with molecules in the gas phase are commonly performed using a molecular beam, which is projected perpendicularly to the incident laser pulses. The laser ionizes the molecular beam in a chamber, usually kept under ultra-high vacuum (UHV), so as to eliminate any interaction with unwanted atoms or molecules. Detection of the photoelectrons can be achieved with a time-of-flight (TOF) spectrometer, referred to as a "magnetic bottle" [29, 30, 31]. The photoelectron kinetic energy spectrum is then calculated from the known electron mass, the length of the magnetic bottle flight path and the measured TOF [29]. Other methods of photoelectron detection are available based on the particular dynamics that wish to be studied [31].

The pump and probe pulses used in TRPES studies are commonly in the UV wavelength range [25, 28], since these photons have the necessary energies required to excite and ionize small molecular systems. Examples of such molecular studies include NO_2 [32, 33] Benzene (NH_3) [34], and Butadiene (C_4H_6). Since most Ti:sa fs lasers operate with a central wavelength of 800nm, it is necessary to use nonlinear frequency mixing techniques in order to obtain the desired UV pump/probe pulses with energies sufficient for ionization of the molecules under study [30]. The generation of these UV wavelengths for TRPES experiments is the topic presented in this thesis.

1.4 – 3rd and 4th Harmonic Generation

Tunable fs laser pulses in the deep ultraviolet range were first observed in the late 1980's and early 1990's with dye lasers using consecutive SFG steps in the nonlinear crystal Beta-Barium Borate (β-BaB_2O_4 or BBO), to produce the 3rd and 4th harmonics of the fundamental laser frequency [35, 36]. The second harmonic beam was mixed in BBO with the fundamental beam to generate the 3rd harmonic, which was subsequently mixed with the fundamental in a second BBO crystal to produce the 4th harmonic. The first 4th harmonic generation experiments in BBO using a Ti:sa CPA fs laser system were performed by Ringling *et al*., who were able to produce radiation between 189-200nm [37].

SFG used for early 4th harmonic generation reused the fundamental beam after each mixing step [35, 36]. This technique maintained reasonable conversion efficiencies for the pulses used, which were >300 fs in duration [35, 36]. However, with shorter pulse lengths, it is not feasible to reuse the fundamental beam for further SFG. The reason for this can be explained with three main phenomena that affect the conversion efficiency in frequency mixing processes.

We must first note that when mixing two pulses of different frequencies, the most efficient summing occurs when the peaks overlap in time. Therefore, spatial/temporal degradation occurs in each pulse being mixed, resulting in a pulse shape resembling that in figure 1.3 a).

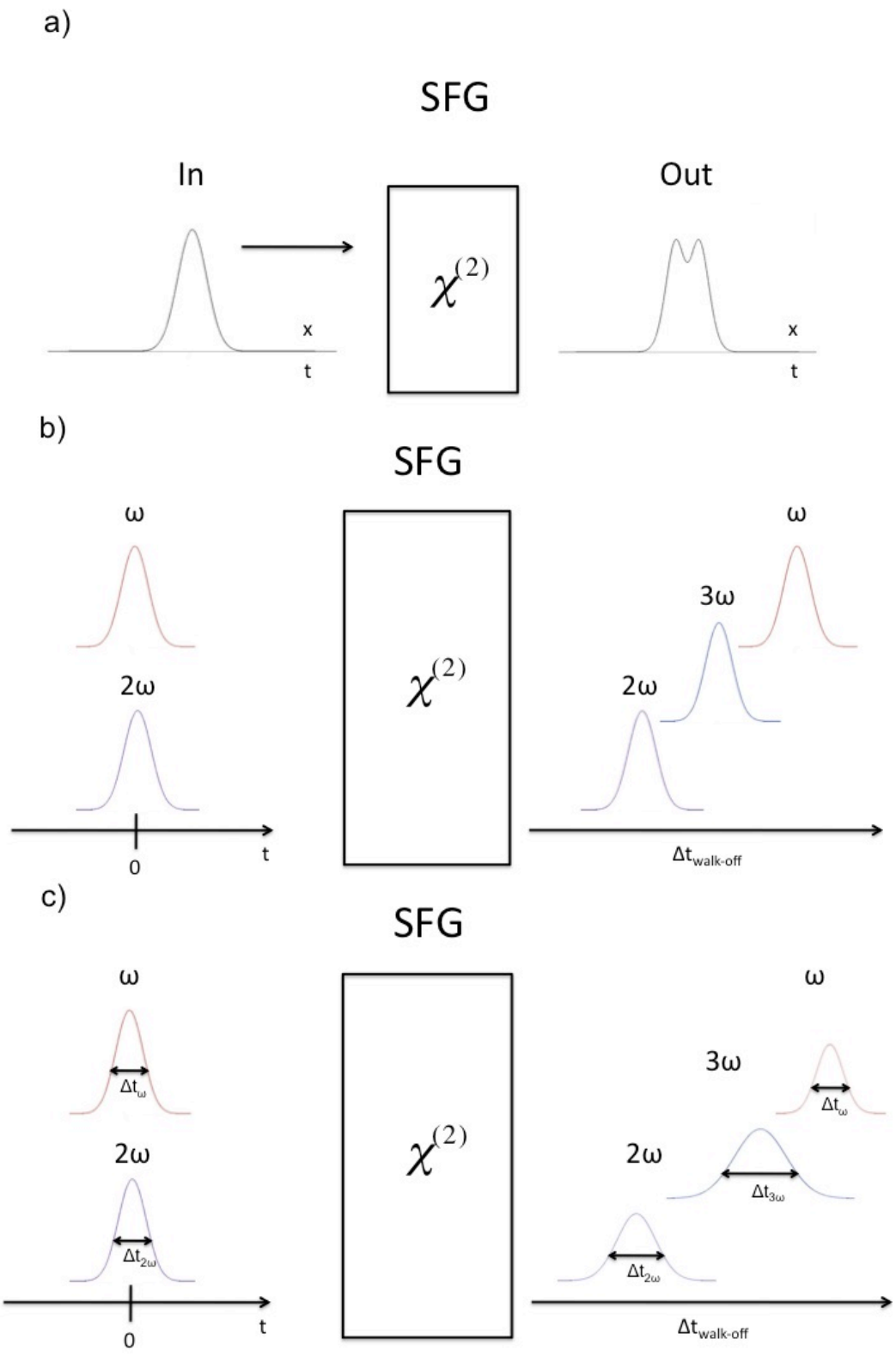

Fig. 1.3 – a) Spatial and temporal degradation occurring in the fundamental pulse after SFG. b) The effects of temporal walk-off in SFG due to the frequency-dependent refractive index. c) Temporal broadening of the output pulses due to GVD in a SFG process. The fundamental pulse experiences the least broadening, while the sum-frequency pulse experiences the most.

Since shorter pulses have higher peak intensities, this effect will be more pronounced than in longer pulses. If the fundamental pulse is reused for the next SFG process, the conversion efficiency will be severely reduced due to the distorted spatial and temporal profile. Thus, it is imperative to split the fundamental beam for fresh use in each SFG step in order to maximize the conversion efficiency. However, doing so reduces the total energy available for each step, so this is only feasible for sufficiently large initial pulse energies. With current commercially available Ti:sa lasers producing pulses on the order of 35fs, it is essential to use new 800nm pulses for each SFG process.

Another factor reducing the conversion efficiency is the temporal walk-off experienced by each pulse in the crystal. Since the index of refraction is a function of frequency, the group velocities of each pulse will not be equal, and as such they will exit the crystal separated in time, as illustrated in figure 1.3 b).

For example, a 35 fs pulse has a spatial length of approximately 10μm, so two pulses of this length will therefore walk-off from one another extremely quickly. As such, thin crystals must be used to reduce this effect [36]. If the temporal walk-off is too great, it will be impossible to reuse the fundamental pulse for further frequency mixing, and a fresh pulse will instead be required.

Group velocity dispersion (GVD) is the third main culprit resulting in a loss in conversion efficiency, however it is not as detrimental as spatial/temporal degradation and pulse walk-off. GVD, which will be discussed in further detail in the following chapter, broadens the temporal envelope of the pulse. Such temporal broadening decreases the peak intensity of the pulse, resulting in less efficient mixing within the crystal, as seen in figure 1.3 c). Furthermore, shorter pulses experience more GVD than longer pulses, which is part

of the reason why early 4th harmonic generation experiments using longer pulse lengths were able to reuse the fundamental beam for successive SFG steps.

In addition to using new portions of the fundamental beam for each SFG process with ultrashort pulses, it is usually necessary to use a collinear geometry, since non-collinear mixing results in significantly lower conversion efficiencies. We can visualize this with figure 1.4, which shows that the interaction region inside of the crystal is considerably larger for a collinear geometry [38]. Moreover, since ultrashort pulses have a very narrow spatial envelope to begin with, the interaction region for non-collinear mixing decreases even more dramatically than with longer pulses.

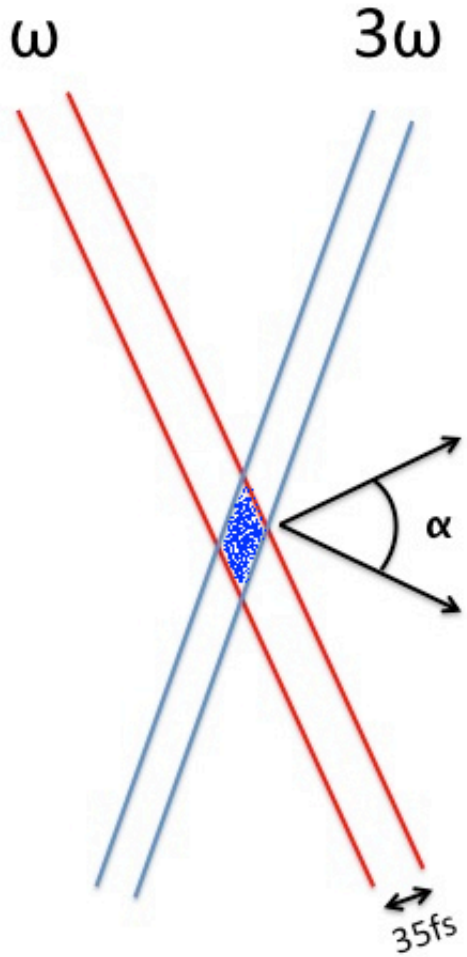

Fig. 1.4 – The significantly reduced interaction region, highlighted in blue, resulting from non-collinear SFG. This is the only area in the crystal where mixing of the two pulses occurs, generating, in this case, the 4th harmonic.

This more preferable SFG setup, which uses a collinear geometry along with new fundamental pulses at each step was performed by Petrov *et al*. [39] and is now the standard method used today for deep UV fs pulse generation.

The experiments discussed in the body of this thesis were performed using this experimental technique to generate the 3rd and 4th harmonics of a mode-locked Ti:sa fs laser system at 266.7nm and 200nm, respectively. Pulses on the order of 100fs have been previously used in the lab to generate these wavelengths, however the current Ti:sa laser system produces pulse lengths of 35 fs. The goal of this project is therefore to generate 266.7nm and 200nm pulses with durations of approximately 35 fs for improved temporal-resolution in TRPES experiments.

The remainder of this thesis is organized as follows: chapter 2 outlines the relevant fundamental nonlinear optical processes with ultrashort pulses, such as SHG, SFG and GVD, leading into a discussion of the initial physical considerations that went into designing the experimental setup. Chapter 3 describes the final design of the 3rd and 4th harmonic generation setup, as well as the experimental techniques used to characterize the generated UV pulses. The performance of the setup and the results of the pulse characterization measurements are presented and discussed in chapter 4, before concluding with a discussion of potential future work and the intended applications of the setup.

Chapter 2: Nonlinear Optics and SFG Simulations

2.1 – Ultrashort Laser Pulses

Ultrashort laser pulses centered at 800nm with durations between 30-100fs are now readily available from commercial laser systems. For the experiments in this thesis, a Ti:sa CPA laser system with pulse lengths of 35fs was used.

There are a few important key features of ultrashort pulses, namely their inherently large peak intensities and broad spectra. The former is a result of the mechanism for ultrashort pulse generation, known as mode-locking, which was outlined in chapter 1. For randomly phased cavity modes, the average laser intensity is the sum of the intensity of the individual modes and is given by [40]

$$\langle I \rangle = M\varepsilon_0{}^2 \Big/ \left(2\sqrt{\mu_0/\varepsilon}\right) \tag{2.1.1}$$

where M is the number of modes oscillating in the laser cavity and ε_0 is the field amplitude of a particular mode. For a mode-locked phase relationship however, the intensity is now equivalent to the product of the intensity of a single mode and the square of the number of modes [40]

$$I(t) = M^2\varepsilon_0{}^2 \Big/ \left(2\sqrt{\mu_0/\varepsilon}\right) \tag{2.1.2}$$

Equation (2.1.2) shows that it is necessary to have a large number of cavity modes in order to generate pulses with high intensities. Since the number of cavity modes is related to the bandwidth, or energy-storage capabilities, of the gain medium, one concludes, as stated in chapter 1, that broadband gain media, such as Ti:sa, are well suited to producing pulses with high peak intensities [40, 41].

Another key feature of ultrashort pulses is their broad spectra, which is fundamentally related to the duration of the pulse. The oscillating electric field of the pulse can be defined in either the temporal or spectral domain, which are related through their Fourier transforms. The full width at half-maximum (FWHM) of the bandwidth, $\Delta\nu_p$, and pulse length, $\Delta\tau_p$, are thus related through the time bandwidth product: [40, 42]

$$\Delta\nu_p \Delta\tau_p \geq c_B \tag{2.1.3}$$

where c_B is a numerical constant on the order of 1 and depends on the shape of the pulse. For Gaussian pulses, which we will be dealing with in this thesis, the value of c_B is 0.441 [40]. It is clear from the form of (2.1.3) that shorter pulses require larger bandwidths. The right hand side of (2.1.3) becomes an equality only if the pulse exhibits the shortest possible duration at a given spectral width and pulse shape [40]. This kind of pulse is known as a transform-limited (TFL), or bandwidth-limited pulse.

2.2 – Fundamental Nonlinear Optical Processes

Prior to discussing the experimental setup that was designed and implemented to generate 200nm pulses, it is important to provide a background explanation of the key nonlinear optical processes involved.

Recall that, as a general definition, a nonlinear optical process is one in which an applied optical field alters the optical properties of a material [41]. The material responds to the applied field in such a way that it shows a nonlinear dependence on the optical field strength [41]. We recall, however, that in order to achieve a nonlinear response, the intensity of the applied field must be sufficiently large, such as that of an ultrashort laser pulse. It is for this reason that femtosecond pulses lend themselves well to nonlinear optical processes.

For example, the electric field of an incident beam of light, E(t), induces a polarization in the material, P(t). This of course corresponds to a physical separation of charge since an applied electric field will exert a force on the electrons. The nonlinear relationship between the material polarization and the applied electric field is well understood, and can be written as a power series in E(t):

$$\tilde{P}(t) = \varepsilon_0 \left[\chi^{(1)} \tilde{E}(t) + \chi^{(2)} \tilde{E}^2(t) + \chi^{(3)} \tilde{E}^3(t) + ... \right] \tag{2.2.1}$$

where ε_0 is the permittivity of free space, $\chi^{(1)}$ is the linear susceptibility of the material, and $\chi^{(2)}$ and $\chi^{(3)}$ are the second and third order nonlinear susceptibilities, respectively. The tildes are used to represent quantities that vary rapidly in time.

The relationship described in equation (2.2.1) is a powerful way to describe nonlinear optical processes. A common nonlinear response of a material is the generation of new frequency components of the incident electric field. The induced polarization is in fact responsible for these new field components, as can be seen when one examines the classical wave equation in a nonlinear optical material:

$$\nabla^2 \tilde{E} - \frac{n^2}{c^2} \frac{\partial^2 \tilde{E}}{\partial t^2} = \frac{1}{\varepsilon_0 c^2} \frac{\partial^2 \tilde{P}^{NL}}{\partial t^2} \tag{2.2.2}$$

where n is the linear refractive index and c is the speed of light in vacuum. The term $\tilde{P}^{NL}$ represents the polarization associated with the nonlinear response of the material and in turn drives the electric field in equation (2.2.2). Furthermore, the second time-derivative of the polarization corresponds physically to a measure of the acceleration of electrons in the material [41]. Classical electromagnetic theory stipulates that accelerating charges emit radiation, so we can see clearly from (2.2.2) that the polarization induced in the material by

the incident electric field in turn facilitates the production of new frequency components of the electromagnetic field.

Second Harmonic Generation

One of the most basic nonlinear optical processes resulting in the generation of a new field component is known as second harmonic generation (SHG). This process is referred to as a $\chi^{(2)}$ process because it occurs in a material, commonly a birefringent crystal, with a non-zero second order nonlinear susceptibility. The second harmonic refers to light generated in the crystal at twice the fundamental frequency, or half the wavelength, of the incident field. SHG is a special case of the more general process known as sum frequency generation (SFG), whereby two input fields at frequencies ω_1 and ω_2 are combined in a $\chi^{(2)}$ material to generate a new field component at frequency $\omega_3 = \omega_1 + \omega_2$. We will first discuss the details of SHG and then continue with a description of SFG.

From the polarization-field description, the second harmonic can be found by applying an electric field of the form

$$\tilde{E}(t) = Ee^{-i\omega t} + c.c \tag{2.2.3}$$

where c.c. denotes the complex conjugate field term, to equation (2.2.1) to obtain an expression for the nonlinear polarization generated in the crystal:

$$\tilde{P}^{(2)}(t) = 2\varepsilon_0\chi^{(2)}EE^* + (\varepsilon_0\chi^{(2)}E^2e^{-2i\omega t} + c.c.) \tag{2.2.4}$$

E^* refers to the complex conjugate of the electric field amplitude, ω is the angular frequency of the field, and c.c represents the remaining complex conjugate terms in the expansion.

The second term in (2.2.4) contains an electric field with squared amplitude at twice the fundamental frequency of the incident field, mathematically demonstrating this particular

nonlinear process. It is of course also important to understand how the process of SHG occurs from a physical standpoint. As introduced above, the key to SHG, and any sort of frequency mixing scheme, lies in the induced polarization of the material, which oscillates under the influence of the incident electric field. When the electric field is very strong, as is the case with laser radiation, the electrons in the material are driven anharmonically, generating additional frequency components that correspond to the harmonics of the fundamental frequency. Thus, in SHG, the polarization has a component oscillating at the frequency of the second harmonic, ω_2, generating a new radiation field at this frequency. Because there are such a large number of atoms in a material sample, the radiation pattern will not be that of typical dipole radiation. Instead, the collection of atoms (atomic dipoles) will oscillate with a phase that depends on the phase of the input beam. If the dipoles are all oscillating in phase (i.e. the polarization is in phase with the generated field), then the fields produced by each oscillating dipole will add constructively in the forward direction. It is easy to see that this process will be extremely inefficient if the dipoles are not oscillating in phase, leading to destructive interference of the generated second harmonic radiation. The specific criterion that allows the correct relative phasing, and thereby the most efficient transfer of energy from the incident to the second harmonic field, is known as phase matching.

Let us examine the phase matching condition in a little more detail. Assuming the general case of (SFG), it is possible to derive an expression describing the fractional change in amplitude of the generated wave at frequency ω_3 with propagation distance through the crystal, z.

This is achieved by inserting the polarization term corresponding to the generated field at frequency ω_3,

$$\tilde{P}_3(z,t) = P_3 e^{-i\omega_3 t} + c.c \tag{2.2.5}$$

into the wave equation (2.2.2), with the amplitude P_3 given by

$$P_3 = 4\varepsilon_0 d_{eff} E_1 E_2 \tag{2.2.6}$$

where d_{eff} is a tensor representing the nonlinear susceptibility of the material. The electric field generated at ω_3 is defined as

$$\tilde{E}_3(z,t) = A_3 e^{i(k_3 z - \omega_3 t)} + c.c \tag{2.2.7}$$

where A_3 and k_3 correspond to the amplitude and wavenumber of the ω_3 field, respectively. From equations (2.2.2), (2.2.5) and (2.2.7) we thus obtain the expression

$$\begin{aligned} &\left[\frac{d^2 A_3}{dz^2} + 2ik_3 \frac{dA_3}{dz} - {k_3}^2 A_3 + \frac{n^2(\omega_3){\omega_3}^2 A_3}{c^2}\right] e^{i(k_3 z - \omega_3 t)} + c.c. \\ &= \frac{-4 d_{eff} {\omega_3}^2}{c^2} A_1 A_2 e^{i[(k_1 + k_2)z - \omega_3 t]} + c.c. \end{aligned} \tag{2.2.8}$$

Since the wavenumber k_3 is defined as

$$k_3 = \frac{n(\omega_3)\omega_3}{c} \tag{2.2.9}$$

we can cancel the third and fourth terms on the left hand side of (2.2.8). Furthermore, the factor of $e^{-i\omega_3 t}$ can be cancelled on both sides of (2.2.8), allowing equation (2.2.8) to be re-written as

$$\frac{d^2 A_3}{dz^2} + 2ik_3 \frac{dA_3}{dz} = \frac{-4 d_{eff} {\omega_3}^2}{c^2} A_1 A_2 e^{i(k_1 + k_2 - k_3)z} \tag{2.2.10}$$

We then make the slowly varying amplitude approximation [41], which states that

$$\left|\frac{d^2 A_3}{dz^2}\right| << \left|k_3 \frac{dA_3}{dz}\right| \tag{2.2.11}$$

This allows us to neglect the leftmost term in (2.2.10), producing the well-known result referred to as a coupled-amplitude equation, which relates the amplitude of the generated field with those of the input fields:

$$\frac{dA_3}{dz} = \frac{2id_{eff}\omega_3^{\,2}}{k_3c^2} A_1A_2e^{i\Delta kz} \tag{2.2.12}$$

where A_1 and A_2 are the amplitudes of the incident waves, and $\Delta k = k_3 - k_1 - k_2$ is a quantity known as the wavevector, or momentum, mismatch.

For SHG, (2.2.12) takes the form

$$\frac{dA_2}{dz} = \frac{id_{eff}\omega_2^{\,2}}{k_2c^2} A_1^{\,2}e^{i\Delta kz} \tag{2.2.13}$$

In this case, conservation of momentum tells us that

$$\Delta k = 2k_1(\omega_1) - k_2(2\omega_1) = 0 \tag{2.2.14}$$

The most efficient transfer of energy from the incident to the second harmonic field occurs when the right hand side of (2.2.14) is equal to zero. This condition is known as perfect phase matching, and it is easy to see that under this circumstance, the amplitude of the second harmonic field increases linearly with propagation distance, z. When perfect phase matching is not achieved, the intensity of the generated field is smaller than for the case of (2.2.14) since not all of the dipoles are oscillating in phase. Furthermore, it can be shown that the intensity of the SH field is of the form

$$I_2 \propto \text{sinc}^2\left(\frac{\Delta kL}{2}\right) \tag{2.2.15}$$

where L is the length of the NLO medium.

Plotting $\text{sinc}^2\left(\frac{\Delta kL}{2}\right)$ against its argument, $\frac{\Delta kL}{2}$, shows how the efficiency of SHG varies with the wavevector mismatch.

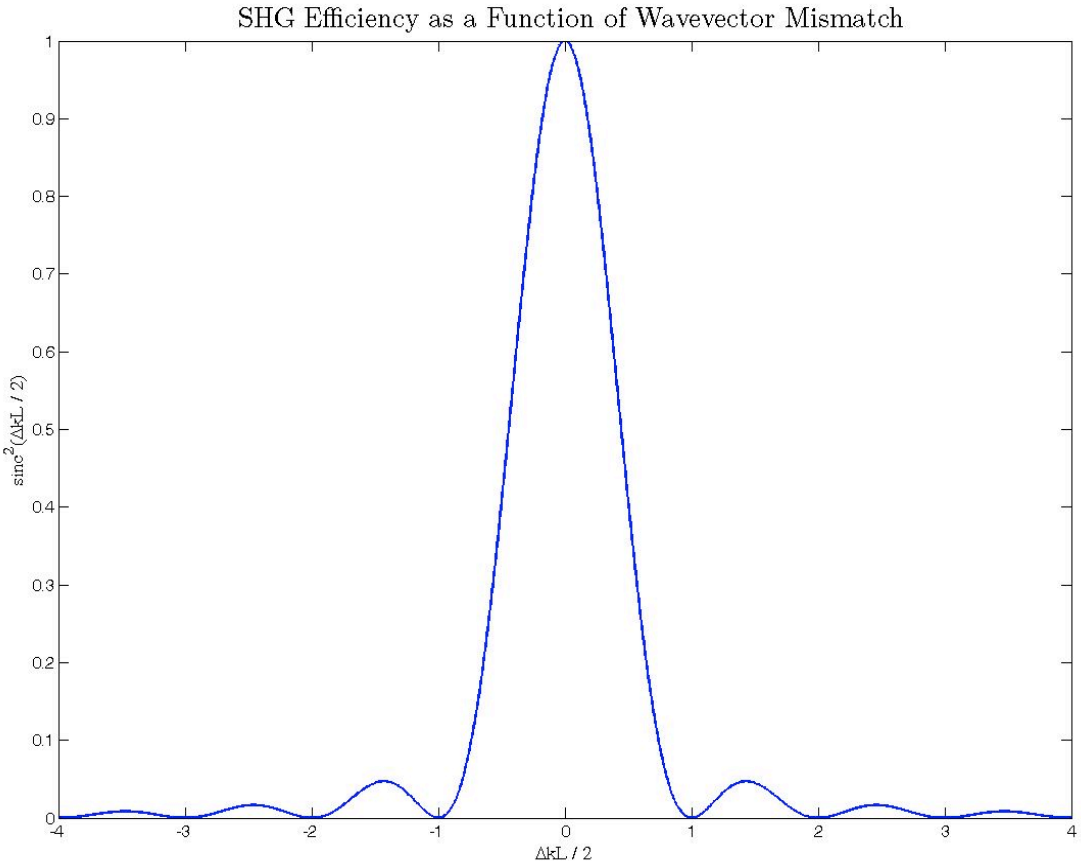

Fig. 2.1 – The intensity of light generated at the second harmonic as a function of wavevector mismatch.

Figure 2.1 illustrates the oscillating dipole picture presented above, demonstrating that the condition of perfect phase matching results in the maximum intensity of the generated $2\omega_1$ field.

However, the above description neglects the effect of normal dispersion, in which the refractive index of the material is an increasing function of frequency. As seen in (2.2.9), the wavevector k is a function of the refractive index of the material:

$$k = \frac{n(\omega)\omega}{c} \tag{2.2.16}$$

From (2.2.16), we can see that the statement of momentum conservation for SHG, given by (2.2.14), requires that

$$n(\omega_1) = n(\omega_2) = n(2\omega_1) \tag{2.2.17}$$

This condition cannot be satisfied if the refractive index increases with frequency, so other means must be employed to compensate for this effect. Fortunately, there are many crystals that display birefringence, allowing for the phase matching of the generated radiation.

Birefringent crystals have one or more axes of symmetry, however most crystals used for frequency mixing processes are uniaxial – they contain only one axis of symmetry. This "optical axis", is defined as the axis along which light with polarization perpendicular to it experiences the ordinary refractive index, n_o, of the material. This beam is referred to as the ordinary ray. However, light with polarization parallel to the optical axis experiences an angle dependent extraordinary refractive index, $n_e(\theta)$, and is known as the extraordinary ray. The angle theta refers to the angle between the optical axis and the direction of propagation of the field, represented by the wavevector $\vec{k}$. Furthermore, uniaxial crystals can be classified as either positive or negative. Positive uniaxial crystals have a larger extraordinary than ordinary refractive index, and vice versa for negative uniaxial crystals.

SHG is commonly achieved with type I phase matching in a negative uniaxial crystal. In type 1 phase matching, ω_1 is polarized such that it acts as the ordinary ray, with refractive index n_o, and $2\omega_1$ is generated with perpendicular polarization, such that it experiences the extraordinary refractive index $n_e(\theta)$. Therefore, for a birefringent crystal, the refractive index felt by the beam with frequency $2\omega_1$ can be adjusted by varying the angle between the beam and the optical axis of the crystal. This phase matching technique is known as angle tuning.

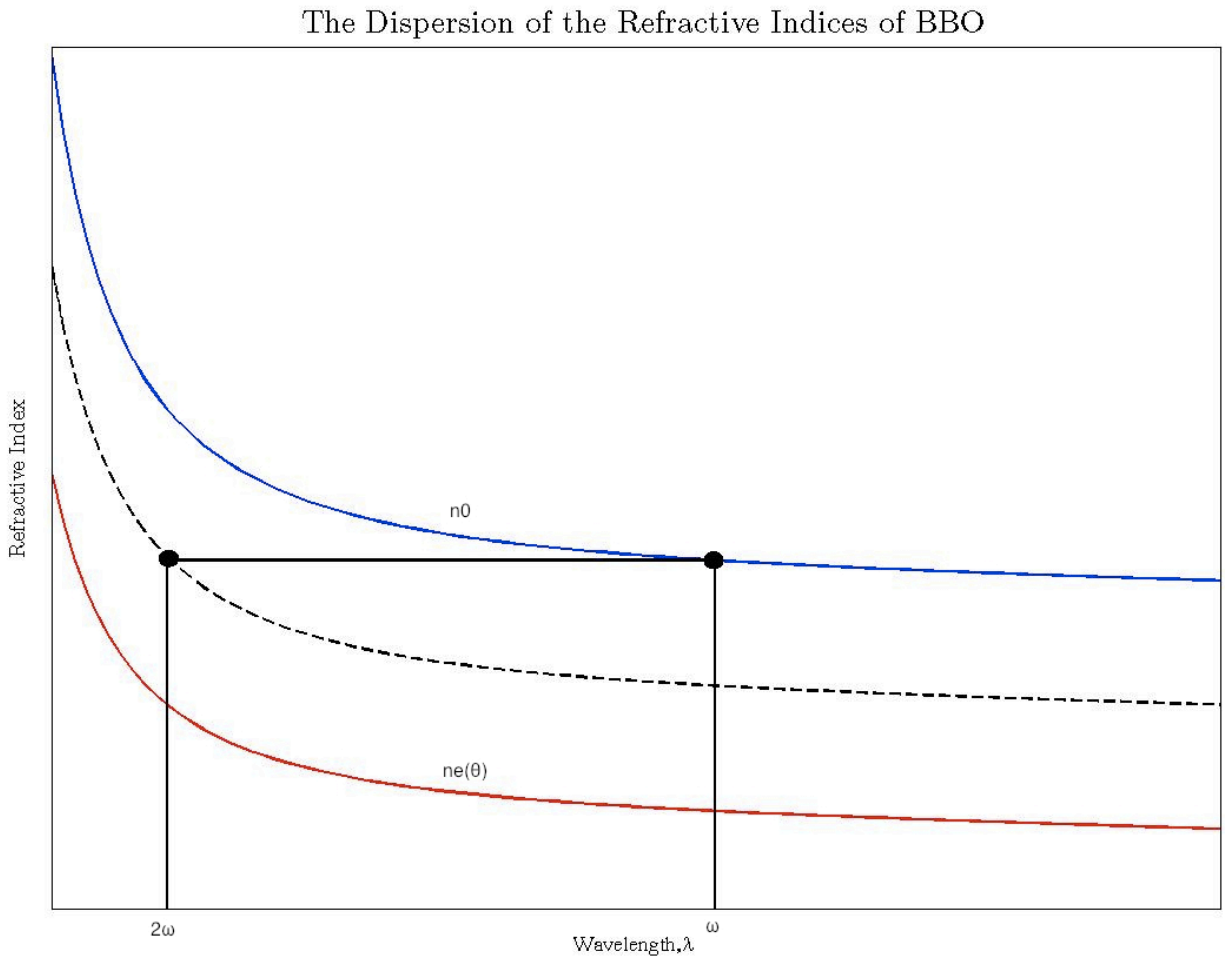

Fig. 2.2 – The dispersion curve for BBO. The dotted line represents the dispersion curve of the new extraordinary refractive index obtained after angle tuning to match $n_e(2\omega)$ with $n_o(\omega)$ for an arbitrary wavelength.

Figure 2.2 helps demonstrate the concrete example of type I angle tuned phase matching for SHG, whereby we generate 400nm light from 800nm light in the negative uniaxial birefringent crystal, BBO. Since the generated field is at a higher frequency than the incident field, it experiences a greater refractive index in the crystal due to dispersion. Therefore the 400nm beam will be travelling more slowly than the 800nm beam and the two beams will be out of phase with each other. However, the polarization of the generated field is always perpendicular to that of the incident field. Therefore, if we select the polarization of the 800nm beam to be perpendicular to the optical axis, the 400nm beam will have a polarization corresponding to the extraordinary ray. By tuning the angle of propagation of

the 400nm beam with respect to the optical axis, one can control the effective refractive index relative to the ordinary refractive index of the 800nm beam until both indices of refraction are as well matched as possible. This phase matching condition follows the form of (2.2.17):

$$n_e(2\omega_1,\theta) = n_o(\omega_1) \tag{2.2.18}$$

and corresponds to the proper phasing of the crystal polarization oscillating at the frequency of the 800nm input beam with the generated radiation at 400nm.

Sum Frequency Generation

The basic physical description of SFG is very similar to SHG. The primary difference is that, in SFG, two input fields at frequencies ω_1 and ω_2 are combined in a $\chi^{(2)}$ material to generate a new field component at frequency $\omega_3 = \omega_1 + \omega_2$. The nonlinear polarization resulting from two input fields, ω_1 and ω_2, is derived in the same manner as (2.2.4) and is found to be

$$\begin{aligned}\tilde{P}^{(2)}(t) = \varepsilon_0\chi^{(2)}[{E_1}^2 e^{-2i\omega_1 t} + {E_2}^2 e^{-2i\omega_2 t} + 2E_1E_2 e^{-i(\omega_1+\omega_2)t} \\ +2E_1{E_2}^* e^{-i(\omega_1-\omega_2)t} + cc] + 2\varepsilon_0\chi^{(2)}[E_1{E_1}^* + E_2{E_2}^*]\end{aligned} \tag{2.2.19}$$

This expression shows that this polarization is able to generate new field components at frequencies $2\omega_1$, $2\omega_2$, $\omega_1+\omega_2$ and $\omega_1-\omega_2$. These frequencies represent the processes of SHG of frequencies ω_1 and ω_2, respectively, SFG and difference frequency generation (DFG).

The oscillating dipole description still holds when depicting the generation of these new frequency components, although from a practical standpoint it is only feasible to generate one of these new field components since it would be quite difficult to achieve the correct phase matching conditions for each process.

2.3 – SHG and SFG Simulations

These phase matching conditions, along with several other physical considerations, had to be addressed prior to the setup of the 200nm source. Initial frequency mixing simulations with the desired input parameters were performed using SNLO, a free nonlinear optical software package from As-Photonics [43] that calculates the correct phase matching angles for the crystals and provides information on the expected energy of the generated light. BBO nonlinear crystals were used for the mixing processes due to their wide transmission and phase matching ranges and their large nonlinear coefficients [36].

The two functions used in SNLO were QMix and PW-mix-SP. QMix first calculates the refractive indices of the fundamental and SH or SF wavelengths in the crystal [43] via the Sellmeier equation [44]:

$$n^2(\lambda) = 1 + \sum_j \frac{B_j \lambda^2}{\lambda^2 - C_j} \tag{2.3.1}$$

where λ represents the incident wavelength, and B_j and C_j are experimentally determined Sellmeier coefficients specific to the optical medium. Typically (2.3.1) contains 3 terms (6 parameters) to account for a broad range of wavelengths [44].

The calculated refractive indices are then used to compute the available phase matching angles for a particular nonlinear crystal at these wavelengths [41]:

$$\frac{\sin^2\theta}{\overline{n}_e(\omega_1+\omega_2)^2} + \frac{\cos^2\theta}{n_o(\omega_1+\omega_2)^2} = \frac{1}{n_o(\omega_1)^2} \tag{2.3.2}$$

QMix also provides values for the group and phase velocities, group delay dispersion and the effective nonlinear susceptibility.

These parameters, including initial pulse energies, pulse durations, beam diameters and crystal thickness are then inserted into the function PW-mix-SP, which calculates the resulting output energies and spectra of three-wave mixing processes for short pulse plane waves. This is achieved through the numerical integration of the wave equation for ultrashort pulses, also known as the nonlinear Schrödinger equation (NLS) [45]

$$\frac{\partial A}{\partial z} = -\frac{ik_2}{2}\frac{\partial^2 A}{\partial T^2} + i\gamma|A|^2 A \tag{2.3.3}$$

where k_2 represents group velocity dispersion (GVD), which is explained in the following paragraph, and $\gamma = 2n_0\varepsilon_0 n_2\omega_0$ is a nonlinear parameter describing nonlinear optical effects such as self-phase modulation (SPM) [45]. SPM is a result of the intensity-dependent nonlinear refractive index, n_2, whereby the refractive index of the material changes with the intensity profile of the pulse and results in spectral and temporal broadening.

The NLS, a nonlinear partial differential equation, does not have a general analytical solution, so PW-mix-SP uses split-step fourier methods to separate the linear and nonlinear components of (2.3.3), which have analytical solutions when treated separately. The linear term, which represents dispersion effects such as GVD, has an analytical solution in the frequency domain and therefore must undergo a fourier transform in order to calculate a solution. The linear and nonlinear terms are thus solved in the frequency domain in two separate steps, recombined, and transformed back to the time domain with an inverse fourier transform [45]. This process is iterated, generating a solution to (2.3.3) which propagates the pulse forward in space and time. The split-step fourier method accurately simulates group velocity effects, which become important for ultrashort pulses due to their inherently broad spectra [43].

Group velocity dispersion (GVD), described mathematically as

$$k_2 = -\frac{1}{v_g^{\,2}} \frac{dv_g}{d\omega}\bigg|_{\omega=\omega_0} \tag{2.3.4}$$

results in spectral and temporal broadening of the pulse. Each spectral component will experience a different refractive index upon propagation through a dispersive optical material, such as a beamsplitter or nonlinear crystal. Therefore, for positive k_2, the long-wavelength components of the spectrum will travel faster than the short-wavelength components, and vice versa for negative k_2, resulting in temporal broadening of the pulse [40,41]. Since longer pulses have lower peak intensities than shorter pulses, the nonlinear mixing process will be less efficient. Furthermore, the temporally stretched pulses limit the desired time resolution required for photoelectron spectroscopy. In addition to GVD, ultrashort pulses also experience temporal walk-off from one another inside of a nonlinear crystal due to the wavelength dependent refractive index. Even when the crystal is tuned to the proper phase matching angle, these effects can still result in a decrease in the efficiency of the mixing process if the crystal is too thick. Therefore, in order to minimize these effects, it is necessary to use thin crystals for SHG and SFG with ultrashort pulses.

However, thin crystals also limit the conversion efficiency of the process since there is less nonlinear material available to facilitate the mixing process. We therefore decided to find a compromise and chose a crystal that was thin enough to facilitate the generation of short pulses with reasonable output energies.

With an available input energy of approximately 750μJ of 800nm light and assuming a beam diameter of 5mm after a 2:1 telescope, we used SNLO to test the resulting output energies and available bandwidth for various crystal thicknesses. For a given crystal thickness, different ratios of the 800nm input beam were tested until we arrived at the

following optimal crystal thicknesses and ratios of incident 800nm light, providing suitable output energies at 400nm, 266.7nm and 200nm:

Wavelength Generated (nm)	**Input Pulse Energy (μJ)**	**Crystal Thickness (μm)**	**Output Pulse Energy (μJ)**
400	390 (800nm) (52% of initial beam)	150	120
266.7	210 (800nm) (28% of initial beam) + 100 (400nm)	50	35
200	150 (800nm) (20% of initial beam) + 25 (266.7nm)	20	1.8

Table 2.1 – Optimal crystal thicknesses as determined from initial SNLO frequency mixing simulations using 52% of the fundamental for SHG, 28% for 3rd harmonic generation and 20% for 4th harmonic generation.

Table 2.2 shows an example of the expected output energies of each wavelength with the same optimal crystal thicknesses as in table 2.1, but with incident 800nm ratios of 50 %, 25 % and 25 % for SHG, and the 3rd and 4th harmonic SFG stages, respectively.

Wavelength Generated (nm)	**Input Pulse Energy (μJ)**	**Crystal Thickness (μm)**	**Output Pulse Energy (μJ)**
400	375 (800nm) (50% of initial beam)	150	115
266.7	187.5 (800nm) (25% of initial beam) + 115 (400nm)	50	30
200	187.5 (800nm) (25% of initial beam) + 30 (266.7nm)	20	1.6

Table 2.2 – Crystal thicknesses as determined from initial SNLO frequency mixing simulations using 50% of the fundamental for SHG and splitting the rest of the 800nm beam equally in the last two SFG steps.

This is a sample step in the iterative process used to determine the optimal mixing conditions.

As mentioned in the introduction chapter, we specifically chose not to reuse the 800nm beam from one mixing step to the next since the fundamental pulse would experience spatial/temporal degradation (figure 1.3 a)) as well as temporal walk-off from the generated pulse (figure 1.3 b)) and broadening due to GVD (figure 1.3 c)). Each of these phenomena will decrease the conversion efficiencies of the subsequent mixing process, resulting in very poor generation of 200nm light since each step would be strongly coupled in this scenario. Even with fresh, short 800nm pulses being used to generate each new wavelength, the conversion efficiencies of the frequency mixing processes decrease from one step to the next. We therefore allotted the majority of the 800nm beam for SHG, which will ensure a

sufficient amount of 400nm light to obtain reasonable conversion efficiencies for the final two SFG stages.

Figure 2.3 is a typical plot of the output data from SNLO comparing the intensities of the SH pulse at 400nm to the 800nm input pulse using the parameters associated with table 2.1. The idler and signal pulses, shown in blue and red respectively, are the same for the case of SHG and the frequency doubled probe pulse is represented in green.

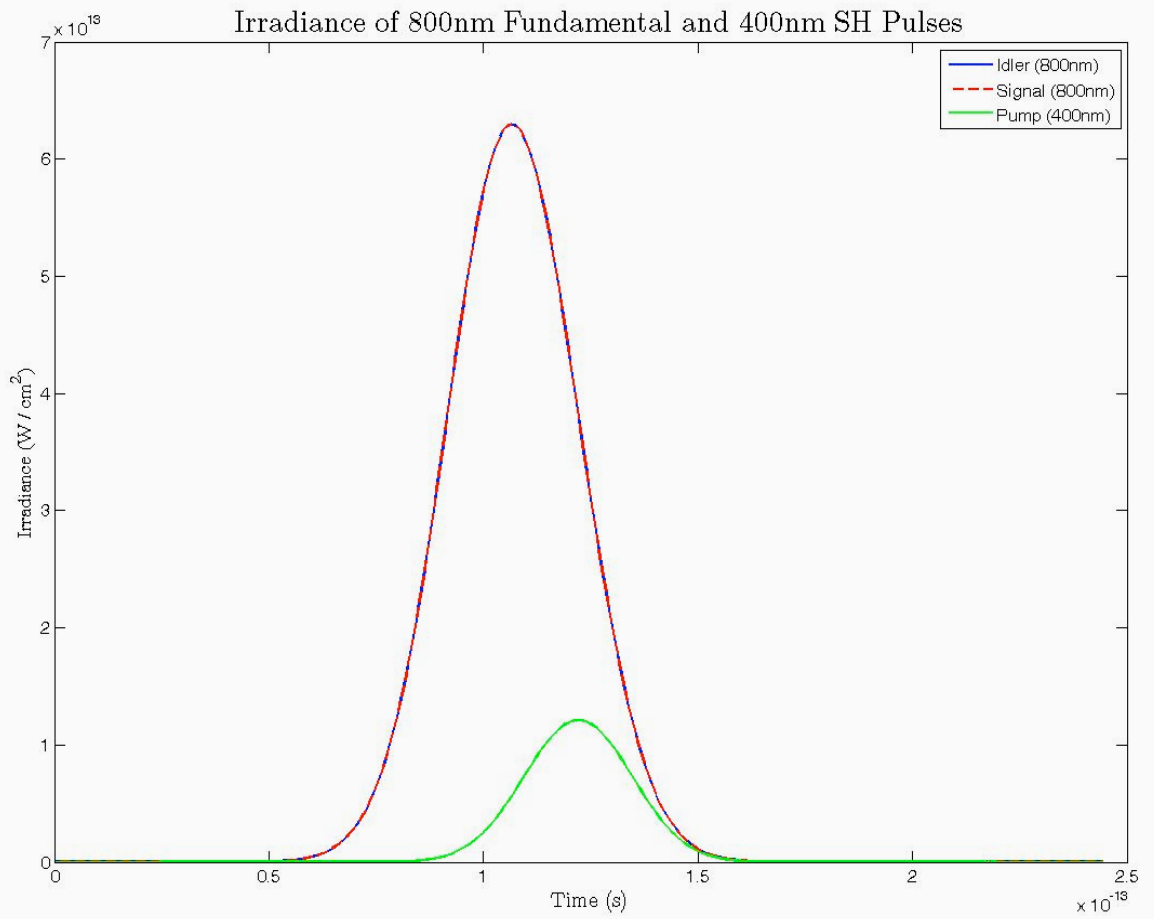

Fig. 2.3 – SNLO simulation of relative intensities of 800nm and 400nm beams after SHG.

Temporal walk-off of the two pulses can be seen, as initially illustrated in figure 1.3 b), with the SH pulse appearing delayed with respect to the fundamental.

Another feature seen in figure 2.3 is the shorter duration of the SH pulse compared to the 800nm pulse, assuming that dispersion effects are minimized. This can be seen from

(2.2.13), which shows that the amplitude of the generated pulse is proportional to the square of the amplitude of the input pulse for the case of SHG. For the general case of SFG, the amplitude of the generated field depends on the product of the two input fields, as seen in (2.2.12). Summing two temporally Gaussian pulses will thus result in the generation of a sum-frequency pulse that is $\sqrt{2}$ shorter than the driving fields. This result applies for SHG as well, where the two input pulses are of the same frequency.

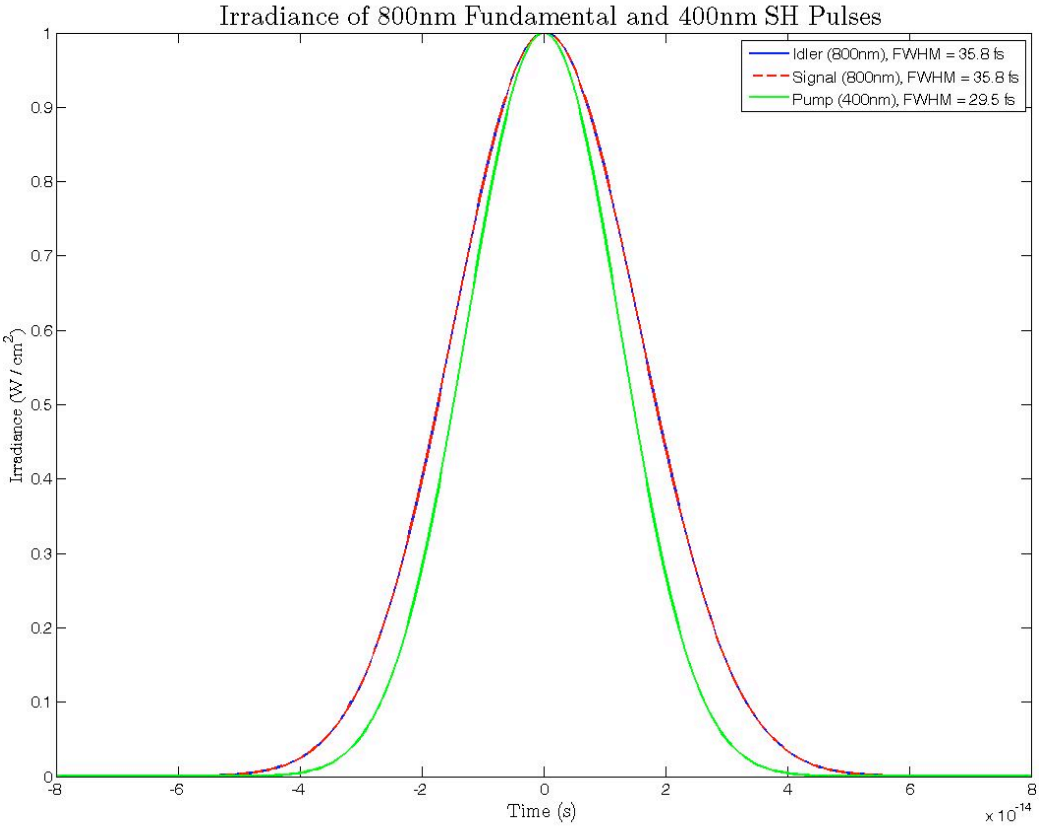

Fig. 2.4 – Comparison of the temporal Intensity profiles of the 800nm fundamental (red & blue) and the 400nm SH (green) pulses.

However, as seen in figure 2.4, the pulse duration of the second harmonic is not actually a factor of $\sqrt{2}$ shorter than the fundamental pulse. This is because the crystal thicknesses were chosen for the best compromise between pulse length and power, so the

interplay between dispersion and the small interaction length in the crystal limit how much shorter the generated pulses can be.

Furthermore, since the SH pulse has a shorter temporal envelope, its spectrum must necessarily be broader, as demonstrated in figure 2.5, which depicts the spectra of the 800nm and 400nm pulses in the frequency domain. The FWHM of the fundamental and second harmonic pulses are 32.9nm and 26.7nm, respectively.

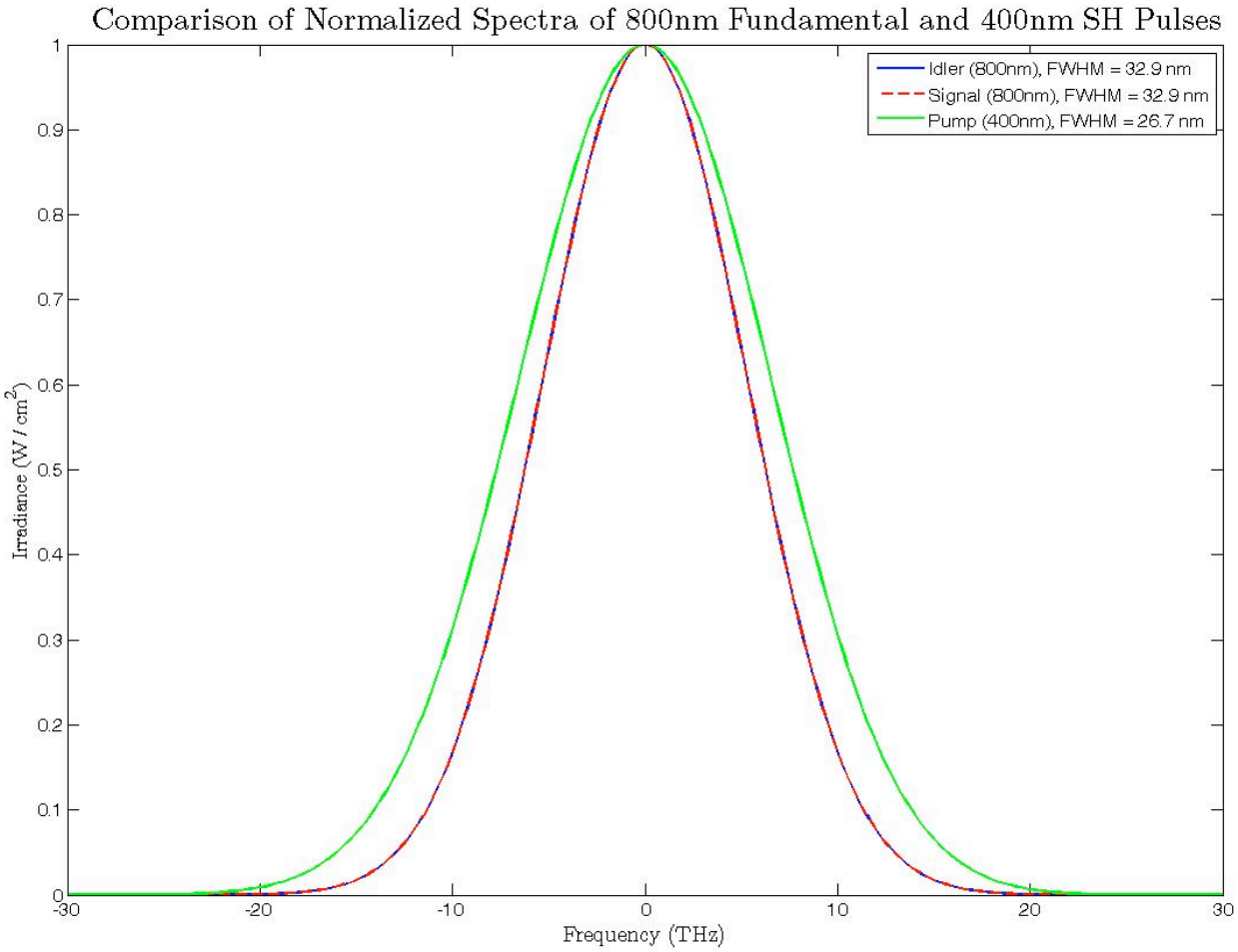

Fig. 2.5 – Comparison of the spectra of the 800nm and 400nm pulses obtained with SNLO, with FWHM values of 32.9nm and 26.7nm, respectively. The signal and idler are both 800nm for the case of SHG shown here.

Figure 2.6 compares the normalized temporal intensity profiles of each wavelength generated in the BBO crystals. Each successively generated pulse is shorter than the

previous one, and will hence have a larger bandwidth. However, it is once again apparent that our necessitated choice of crystal thicknesses does not facilitate a $\sqrt{2}$ decrease in pulse duration.

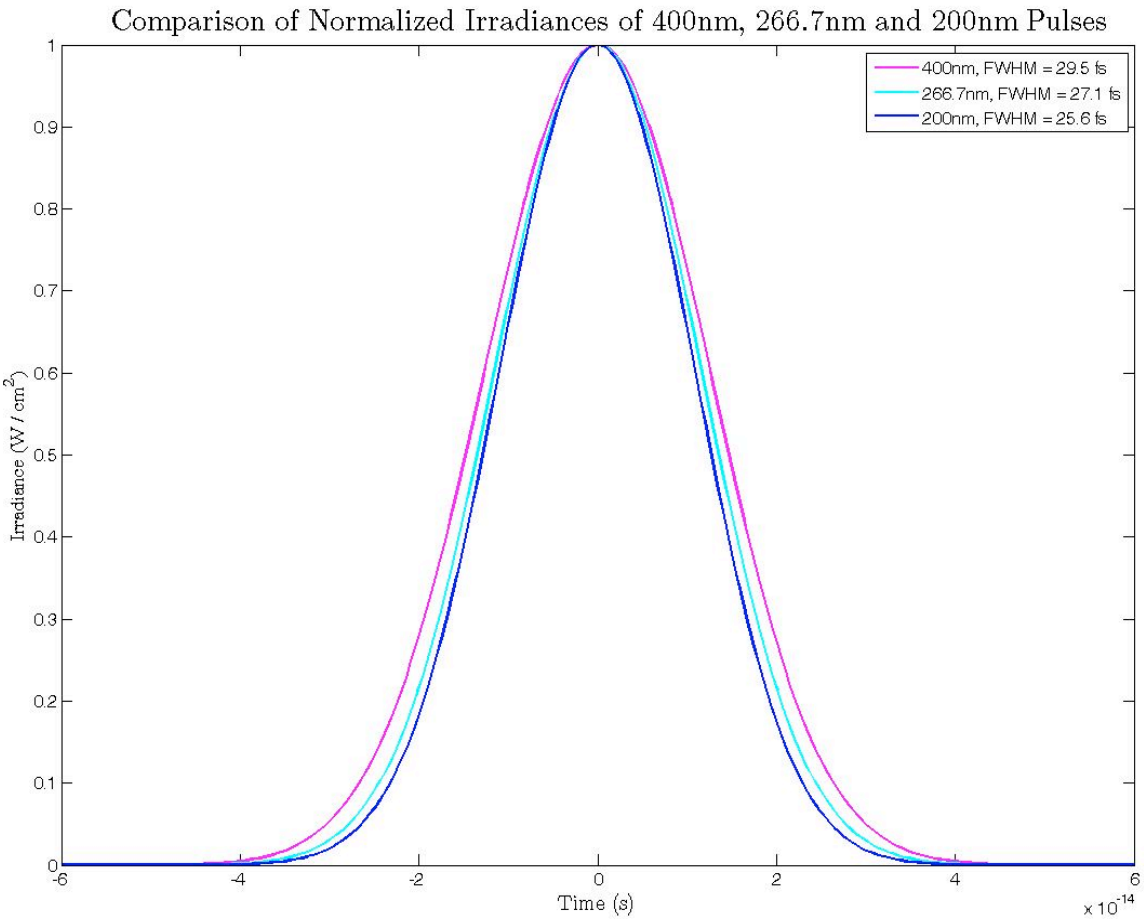

Fig. 2.6 –Temporal intensity profiles of each of the generated UV fs pulses.

Now that we have discussed the fundamental nonlinear optical processes involved in this work, our attention will turn to a detailed description of the experimental setup constructed to generate the 266.7nm and 200nm pulses.

Chapter 3: Experimental Design of 3rd and 4th Harmonic Generation Setup

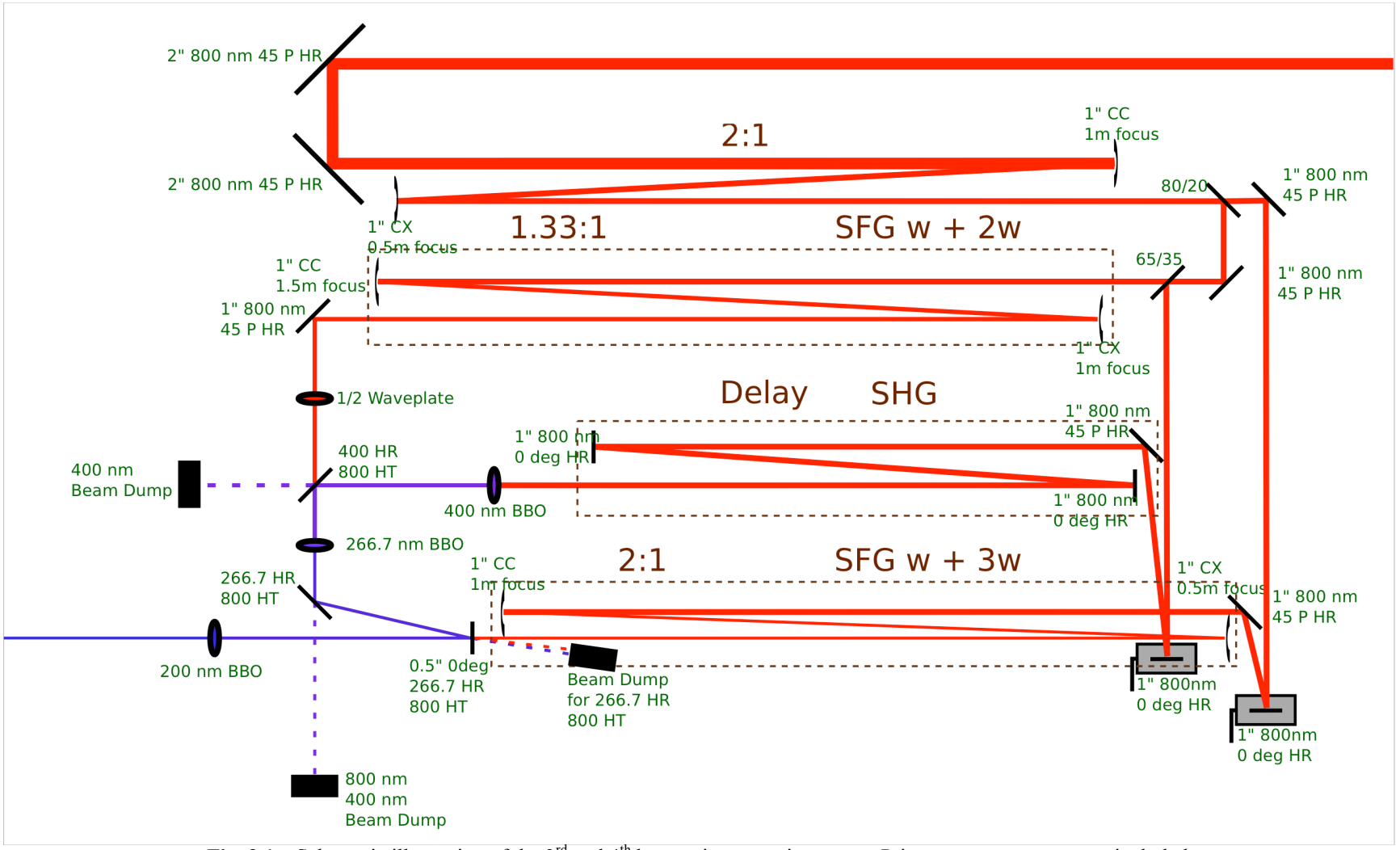

Fig. 3.1 – Schematic illustration of the 3rd and 4th harmonic generation setup. Prism compressors are not included.

3.1 – Overview of Experimental Setup

The 200nm generation setup along with prism compressors for the 266.7nm and 200nm beams was assembled on a 600mm x 1200mm Newport optical breadboard with M6 metric hole spacing. Figure 3.1 illustrates the experimental setup, without the inclusion of prism compressors.

The beam used for the setup was generated by a Ti:sa mode-locked CPA laser system from Coherent, centered at 800nm, operating at a pulse repetition rate of 1kHz. The amplifier system (Coherent Legend Elite Duo) consisted of a regenerative amplifier, followed by a single pass amplification stage. The output of the amplifier was split into two, where half seeded a cryogenic amplifier and the other half was compressed, resulting in a final output pulse energy of around 3.7 mJ and a beam diameter of about 10 mm. The beam was then split and directed to several different experimental setups, providing the 200nm generation source with an input pulse energy of around 730μJ per pulse.

The 3rd and 4th harmonic setup was initially seeded with the cryogenic amplifier, which provided pulse energies of around 8.3mJ and a beam diameter of about 16mm. However, it was decided that this amount of amplification was not necessary for the purposes of this work, so the Legend Elite Duo was used for the remainder of the project.

As shown in figure 3.1, the input beam passed through a 2:1 reflective telescope. The concave (CC) mirror had a focal length of 1m, and the convex (CX) mirror had a 0.5m focal length. The distance separating the mirrors was then determined by the sum of their focal lengths:

$$d = f_1 + f_2 \tag{3.1.1}$$

For the case of the first telescope, the mirror separation distance should be 0.5m, reducing the beam diameter from 10mm to 5mm. Reflective telescopes were used in the setup as opposed to transmissive lens telescopes in order to avoid astigmatism in the beam as well as significant pulse lengthening due to GVD, both of which would affect the conversion efficiencies in each BBO crystal. After the first telescope, the beam then passed through a 45˚ 80/20 beam splitter. 80% of the beam was reflected and directed to a 45˚ 65/35 beam splitter and 20% of the beam was transmitted and sent to the 3rd telescope for 200nm generation. Upon encountering the second beam splitter, 65% of the beam was reflected and sent to the SHG crystal, and 35% of the beam was transmitted and sent to the 266.7nm generation crystal. Therefore, approximately 52% of the total input beam was used for the SHG step, 28% was used to generate the 266.7nm light, and 20% was allocated for the 200nm generation, as outlined in table 2.1.

It is essential that the beamsplitters be mounted correctly. As a rule of thumb, the beamsplitter is oriented such that the greater portion of the beam is reflected, while the lesser portion is transmitted through the optic. The side with the beamsplitting coating is determined by placing the beamsplitter in the beam path, blocking the transmitted portion of the beam, and then measuring the energy of the resulting reflected portion of the beam. The initial beam energy is known, so based on the measured energy, we can deduce which side has the greater splitting ratio and mount the optic accordingly. In order to optimize the performance of the beamsplitter, the optic is rotated about the axis of the mount while monitoring the reflected energy with a power meter until the maximum is obtained.

The crystals used for frequency mixing were, as determined from the QMix function in SNLO, a 7mm x 7mm x 0.15mm BBO with a cut angle of 29.2˚ for SHG, a 7mm x 7mm x 0.05mm BBO with a cut angle of 44.3° for SFG to 266.7nm and a 7mm x 7mm x 0.02mm

BBO cut at 64.8° for SFG to 200nm. Each nonlinear mixing process was achieved with type I phase matching. Figure 3.2 shows each of the nonlinear crystals used in the 200nm generation setup.

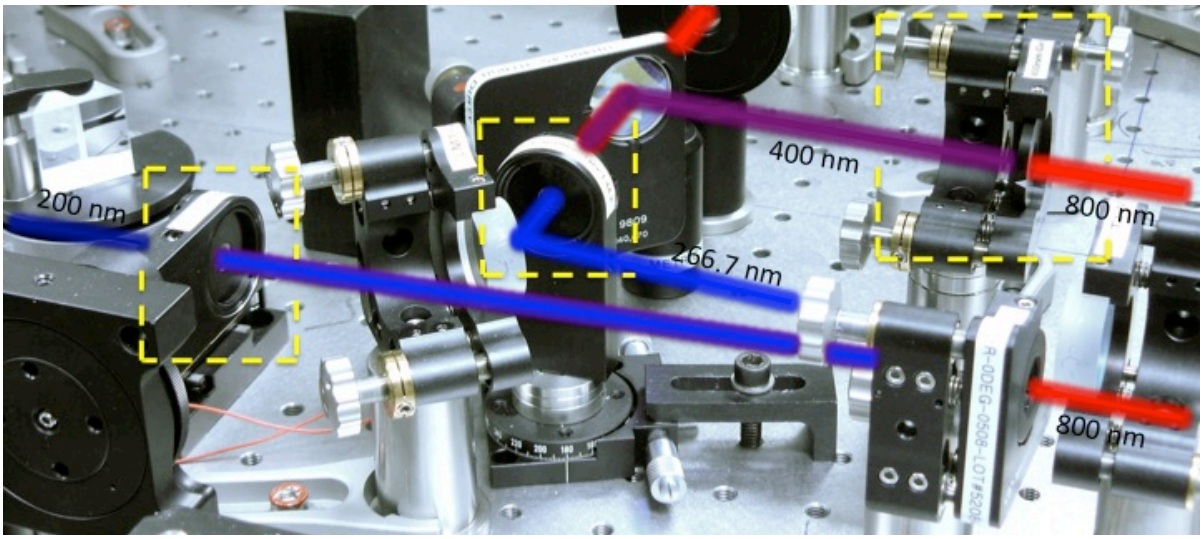

Fig. 3.2 – The three nonlinear BBO crystals used for 400nm, 267nm and 200nm generation.

Due to conservation of momentum and assuming a Gaussian beam profile, the beam diameter should decrease after each nonlinear mixing process by a factor of $\sqrt{2}$. This can be explained in the same manner as for the decrease in pulse length upon SFG: summing two spatially Gaussian pulses will result in the generation of a sum-frequency pulse with a beam diameter that is $\sqrt{2}$ smaller than the driving fields. The interacting pulses must of course have the same spatial widths in order for the diameter of the resulting pulse to be reduced by the factor of $\sqrt{2}$. The 400nm beam will then be smaller than the 800nm beam that it recombines with to generate the 3rd harmonic. In order to maximize the conversion efficiency of this SFG process, the 800nm beam must be telescoped down to match the diameter to the SH beam. Similarly, the 800nm beam used for the 200nm SFG process is telescoped down with a reflective telescope in order to match its diameter to that of the 266.7nm beam.

3.2 – Beam Spot Sizes

The beam diameters were measured using an iris and an Ophir 3A-FS power meter. The iris was closed until 86% of the full beam power was transmitted, at which point the diameter of the aperture was measured with vernier calipers, which have an uncertainty of ± 0.05mm. This diameter corresponds to the beam spot size [46]. Tables 3.1 and 3.2 list the measured spot sizes of each wavelength from the output of the cryogenic amplifier and the Legend Elite Duo amplifier, respectively.

Wavelength (nm)	**Nonlinear Mixing Stage**	**Beam Diameter (mm)**
800	(SHG)	8.2 ± 0.05
800	(266.7nm SFG)	6.8 ± 0.05
400	(266.7nm SFG)	7.0 ± 0.05
800	(200nm SFG)	5.3 ± 0.05
266.7	(200nm SFG)	5.0 ± 0.05
200	N/A	4.8 ± 0.05

Table 3.1 – Measured beam diameters of each wavelength from the cryo amplifier.

Wavelength (nm)	Nonlinear Mixing Stage	Beam Diameter (mm)
800	(SHG)	5.5 ± 0.05
800	(266.7nm SFG)	4.0 ± 0.05
400	(266.7nm SFG)	3.8 ± 0.05
800	(200nm SFG)	2.8 ± 0.05
266.7	(200nm SFG)	2.8 ± 0.05
200	N/A	2.0 ± 0.05

Table 3.2 – Measured beam diameters of each wavelength from the Legend Elite Duo regenerative amplifier.

3.3 – Spatial Overlap: Telescopes

As seen in tables 3.1 and 3.2, the diameters of the 800nm beams used for the SFG steps are fairly well matched to their respective UV beams. The performance of the experimental setup varied significantly for each set of beam diameters used, which will be discussed in the following chapter. In order to achieve the overlap for the 266.7nm stage, a 1.33:1 reflective telescope was required to reduce the diameter of the 800nm beam to match that of the second harmonic. The CC mirror had a focal length of 2m, and the CX mirror had a focal length of 1.5m, resulting in a desired mirror separation of 0.5m. The third, and final, telescope used for the 200nm generation stage had a 2:1 ratio resulting from a CC mirror with a 1m focal length and a CX mirror with a 0.5m focal length. The mirror separation distance should again be 0.5m. Collimation of the beams was checked and confirmed after each telescope over a distance of around 3-4m. Divergence in any of the beams as they enter

the crystal hinders the efficiency of the frequency mixing process due to a reduction in the available phase matching acceptance angle [38], and should thus be avoided. Figure 3.3 shows each of the telescopes in the setup.

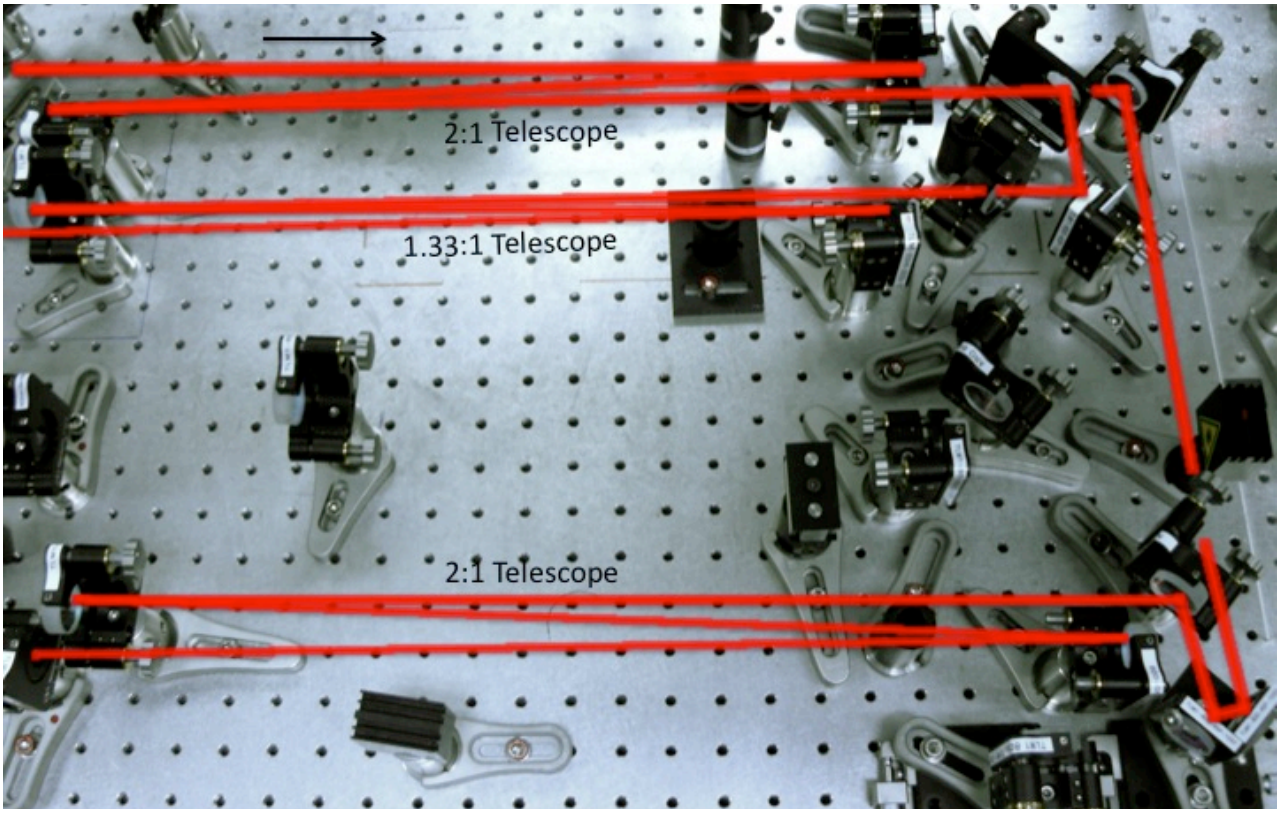

Fig. 3.3 – The three telescopes used to initially decrease the spot size of the beam entering the SHG crystal and then to match the spot sizes of the overlapping beams in the two SFG stages.

3.4 – Temporal Overlap: Translation Stages

In order for the nonlinear mixing processes to occur in the crystals, the beams must be overlapped not only in space but also in time. The spatial overlap was ensured with the telescopes, while the temporal overlap was achieved with two hand-adjustable micrometer translation stages. The leftmost stage in figure 3.1 controlled the temporal overlap required to generate the 3rd harmonic, and the stage to the right was used for 4th harmonic generation. Figure 3.4 shows the translation stages from the completed setup.

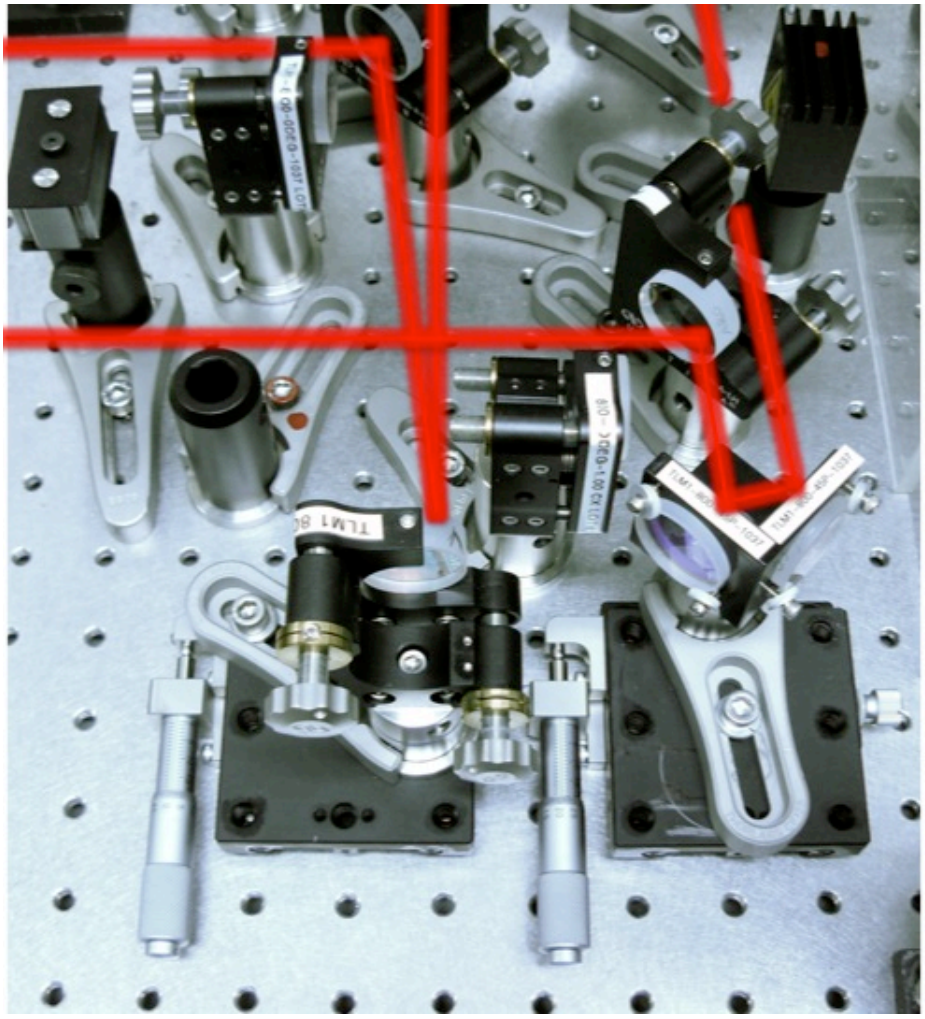

Fig. 3.4 – The translation stages used to control the arrival time of the 800nm pulses in each of the SFG arms.

3.5 – Polarization Matching: Periscope for 200nm Beam

Another important consideration that was made when designing the setup was the polarization of the beams entering each crystal. The 800nm fundamental beam emitted from the regenerative amplifier was P polarized. That is, its electric field was parallel to the plane of incidence of a reflecting surface. As discussed in chapter 2, the polarization of the light incident on a nonlinear birefringent crystal is very important, as it determines the polarization state of the generated wavelength. After passing through the SH crystal, the polarization of the emitted 400nm light was rotated by 90˚ to the S state. In other words, the

electric field is now perpendicular to the reflective plane of incidence. In order for SFG to 266.7nm to occur with type I phase matching, the 800nm and 400nm beams must share the same polarization state. It is therefore necessary to place a $\lambda/2$ waveplate in the path of the 800nm beam to rotate its polarization from P to S. The nonlinear mixing process will then generate 266.7nm light with P polarization, which recombines with the initially P polarized 800nm light to produce the final 200nm beam with S polarization.

However, P polarized light is in fact desirable for pump-probe experiments, and the reflection losses are minimized for this polarization in the prisms that pre-compress the pulses [47], so the polarization of the 200nm pulses must therefore be changed from S to P. We accomplished this with a simple periscope setup, as seen in figure 3.5.

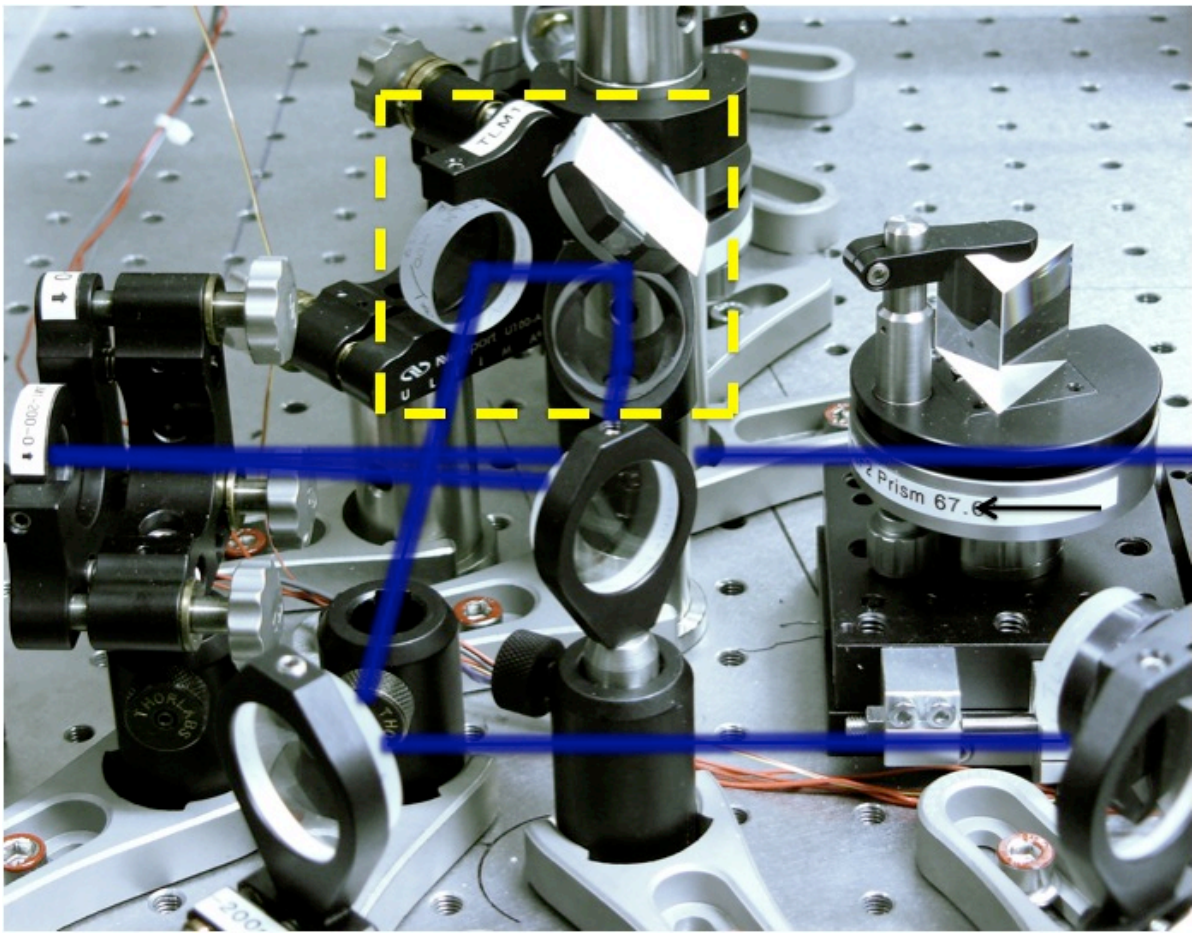

Fig. 3.5 – P-polarizing periscope for the 200nm beam.

3.6 – Pulse Compression: Prism Compressors

Each frequency component of the pulse experiences lengthening due to GVD as it passes through the setup. For example, the 800nm beam from the Duo amplifier passes through a beamsplitter before entering the 4th harmonic setup. Once inside, the beams pass through the BBO crystals, the $\lambda/2$ waveplate, and the 3rd harmonic passes through a 200nm dichroic high reflector in order to separate the both beams, which are collinear upon exiting the final BBO crystal. The final pulses will therefore be longer than the desired duration of 35fs. In addition, the pulses must be recombined with dichroic high reflectors and will pass through a window when entering a vacuum chamber for TRPES experiments, resulting in further temporal broadening. All of these dispersion effects must therefore be pre-compensated for such that upon entering a spectroscopic experiment, the pulses are around 35fs in duration.

As will be discussed in chapter 4, the spectral width of each wavelength determines the shortest possible pulse length according to the time-bandwidth product. We can then use a pair of CaF_2 prisms to compress the pulses to the shortest possible duration, preparing them for an experiment. Using a pulse propagation simulation written in Matlab, the Brewster cut angles of each prism pair were determined to be 68.7° and 67.6° for the 266.7 and 200nm pulses, respectively. This Matlab code was also used to calculate the geometry of the prism compressors required for optimal compression, the details of which will be discussed in the following chapter. Figure 3.6 shows the prism compressor setup for both the 266.7nm and 200nm beams.

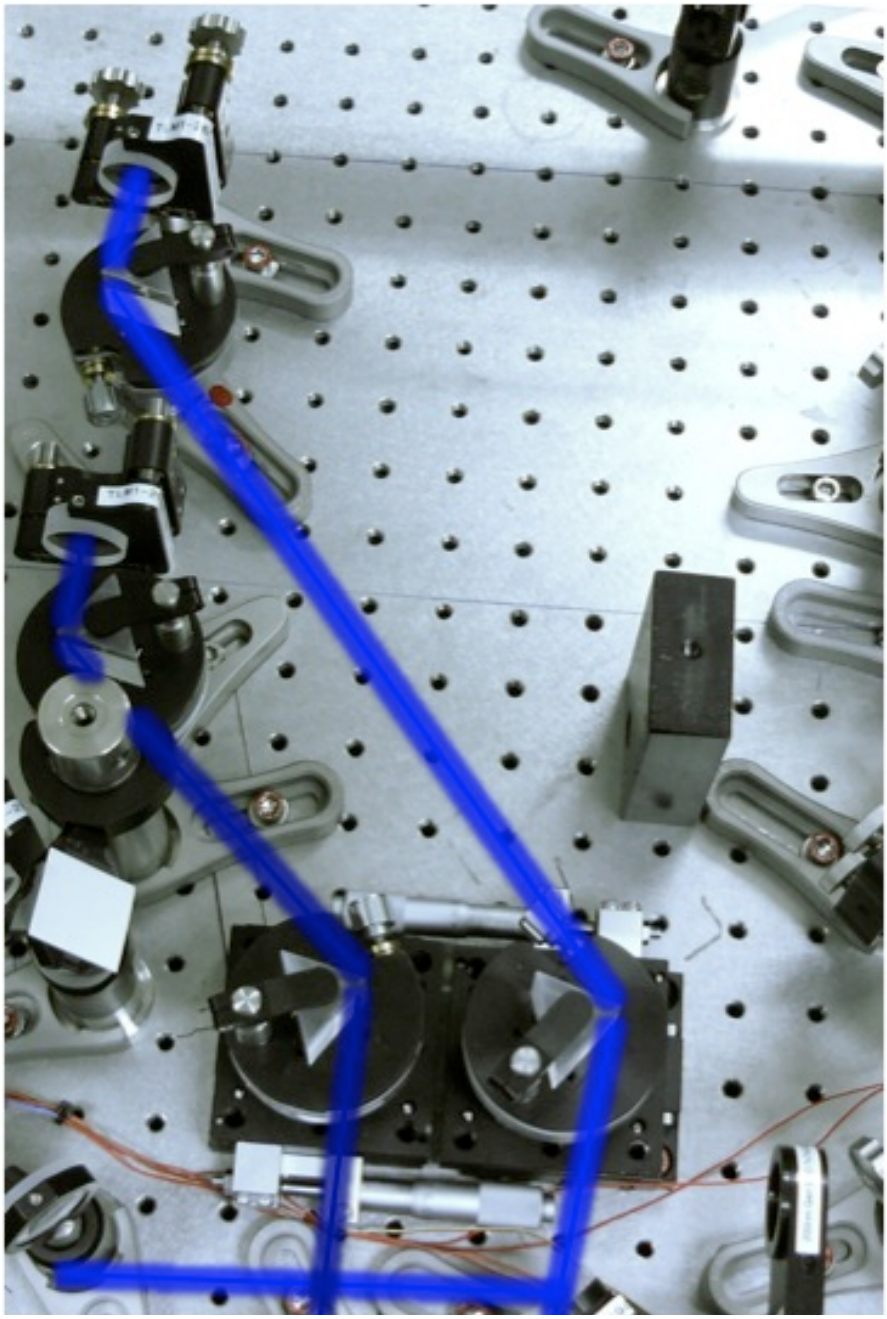

Fig. 3.6 – Prism compressors for the 267nm and 200nm pulses prior to exiting the setup.

The apex angle of each prism corresponds to the Brewster angle for that particular wavelength and each beam enters and exits the prism at its respective Brewster angle in order to minimize loss in the material [47]. The pulse then experiences dispersion as it passes through the material and the different spectral components are refracted as in figure 3.7.

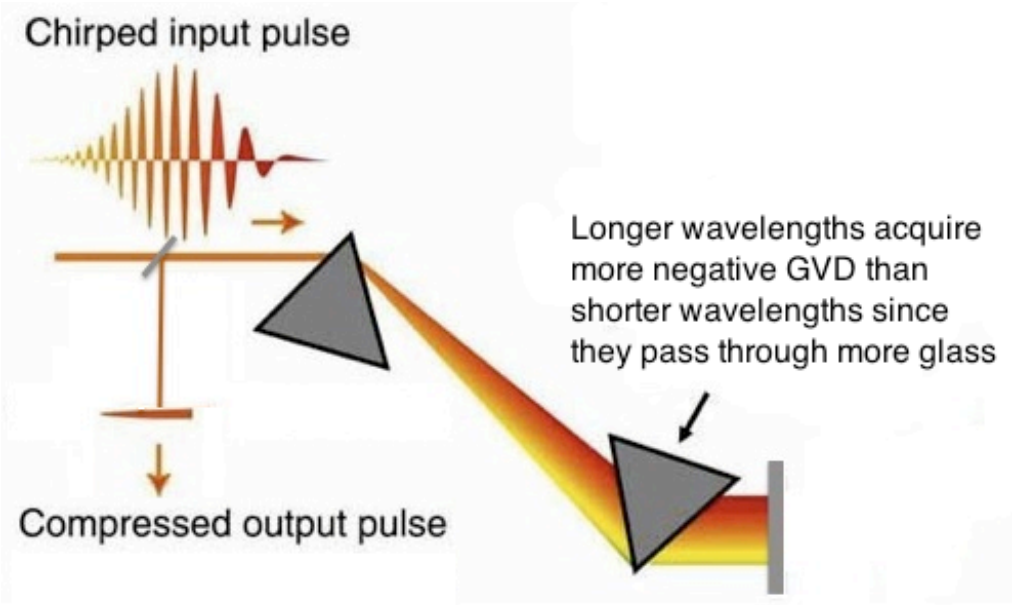

Fig. 3.7 – A typical double pass prism compressor setup. The red lines represent spectral components of shorter frequency and the yellow lines represent higher frequency components [48].

As shown by Martinez *et al*. [49], angular dispersion such as that introduced by a pair of prisms inherently results in negative GVD, regardless of the sign of the material dispersion. Therefore, the positive material dispersion can be compensated for by the negative GVD.

If the incident pulses have travelled through a finite amount of material prior to the compressor, they will have experienced positive GVD and consequently been stretched temporally due to the separation of spectral components. Longer wavelengths will therefore be shifted to the front of the pulse, while shorter wavelengths appear at the rear. Upon entering the first prism, each frequency component begins to experience both positive material dispersion, as well as negative GVD. The longer wavelengths will be refracted at a more shallow angle than shorter wavelengths and will consequently enter the second prism at an earlier time. Because of the negative GVD experienced by the pulse, the longer wavelengths will in fact travel through the prism more slowly than the shorter wavelengths.

This greater distance observed by the longer wavelengths through the second prism will result in further acquisition of negative GVD and, upon reflection by a mirror back through the prism pair, the spectral components will find themselves in their original, unaltered locations within the pulse envelope.

One other important parameter in the compressor is the apex-apex separation distance of the prisms. This distance travelled by the beam in air increases the amount of negative GVD experienced by the beam, as shown by [49, 50]. Therefore, by changing the prism separation distance, it is possible to adjust the amount of GVD affecting the pulses to either exactly compensate for any previous positive GVD, or to leave the pulse with a certain amount of negative GVD to pre-compensate for the dispersion experienced upon passing through a window into a vacuum chamber.

Each prism compressor was set up one prism at a time. The beam was sent into the first prism, which was mounted on a micrometer translation stage, and the unit was then rotated until the angle of minimum deviation experienced by the beam was found. The prism remained fixed at this angle and was moved in or out of the beam path with the translation stage until the beam was as close to the apex as possible without clipping. It is important that the prism is aligned parallel to the mount's axis of translation, so that the angle of deviation of the beam does not change as the prism is moved.

With the first prism in place, the second prism was positioned at the appropriate distance. It was again rotated until the angle of minimum deviation was found, at which point it was carefully translated horizontally by hand to bring the beam as close to the apex as possible without clipping. Finally, a 0° HR was placed after the second prism to send the beam back through the compressor in the same vertical plane, but slightly below the input

beam. The compressed beam was then directed out of the setup with a dichroic HR pickoff mirror.

The duration of the 800nm pulses before the input to the setup was measured to be 34-35 fs using a single shot autocorrelator setup. Upon entering the autocorrelator, the 800nm beam was split in two and then recombined non-collinearly in a BBO crystal for SHG. The SH signal resulting from the angled overlap in the crystal was detected with a linear photodiode array and sent to Thorlabs Inc. Usb line camera software. The FHWM of the autocorrelation trace, and thus the pulse length, can be determined through calibration of the setup.

In order to compress the 3mm, 266.7nm pulses back to durations of 35 fs, the apex-apex distance of the prisms was calculated to be roughly 30cm. The 200nm beam has a spot size of about 2 mm, and the required prism separation distance was calculated to be approximately 16 cm to regain pulses of 35 fs in duration. In order to ensure that the pulse durations have been minimized, the beams must be directed into an intensity autocorrelator for temporal characterization upon exiting the setup. Once optimal compression has been achieved, the 3rd and 4th harmonics are ready to be sent to a vacuum chamber for pump-probe experiments.

3.7 – Pulse Length Characterization: TPA Intensity Autocorrelator

Prior to performing a spectroscopic experiment, it is desirable to have a thorough understanding of the characteristics of the light being used to excite the molecules under study. This knowledge will provide an idea of the nature of the expected results and perhaps

whether or not it is even possible to observe the desired phenomenon based on the duration of the laser pulses.

Measurements of the energy, spectrum and spatial profile of the laser pulse are fairly straightforward. However, it is not as trivial to measure the temporal profile of an ultrashort laser pulse since current electronics are unable to sample a signal in real time on the femtosecond time scale. One must therefore resort to inference techniques that can provide information about the pulse duration. A common, well-established method is the intensity autocorrelation [51, 52], which was used to measure the temporal profiles of the pulses generated in this setup.

This method provides information about the duration of the pulses in question, but does not offer any information about the spectral phase, or chirp, of the pulse as with other characterization techniques such as frequency-resolved optical gating (FROG) and spectral phase interferometry for direct electric-field reconstruction (SPIDER) [53, 54, 55]. However, information about the spectral phase is not required for the purpose of optimally compressing the pulses, making the intensity autocorrelator an ideal tool for our setup.

Two-photon absorption (TPA) is the underlying physical mechanism at work in this technique. It is a third order, or χ^3, nonlinear optical process whereby an atom simultaneously absorbs two photons of either the same or different frequencies, resulting in a transition to an excited electronic state.

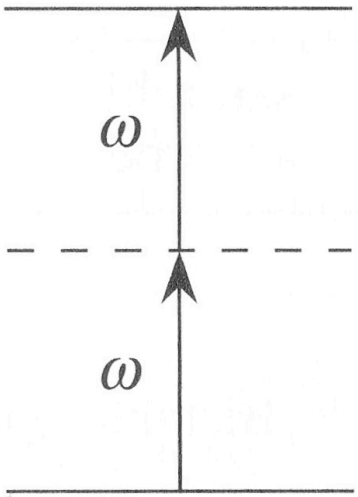

Fig. 3.8 – Energy level diagram of TPA [41].

The energy difference between these two states is equal to the sum of the energies of the individual photons. The autocorrelation measurements performed with our setup inherently used photons of the same frequency.

The atomic transition rate, R, that results from TPA is described as

$$R = \frac{\sigma I}{\hbar\omega} \tag{3.7.1}$$

where σ is the absorption cross section describing the process in terms of photons cm^{-2} sec^{-1} and I is the laser intensity [41]. The absorption cross section is in turn written as

$$\sigma = \beta I \tag{3.7.2}$$

where β is known as the TPA coefficient describing the strength of the process. Combining 3.7.2 and 3.7.1 leads to the conclusion that the TPA process depends on the square of the laser intensity.

$$R = \frac{\beta I^2}{\hbar\omega} \tag{3.7.3}$$

TPA therefore occurs quite readily when the medium is excited with ultrashort laser pulses due to their inherently large peak intensities, as discussed in chapter 2.

TPA is observed in many liquids and bulk materials, even for relatively low energy femtosecond pulses on the order of several to a few hundred nJ, as long as the photon energy is greater than half of the band gap energy [56, 57]. In addition to the intensity dependence seen in (3.7.3), TPA is also advantageous when performing an autocorrelation measurement with UV pulses since no phase matching conditions are required. Techniques such as FROG and SPIDER inherently rely on nonlinear frequency mixing such as SHG and SFG in order to extract temporal and spectral phase information about the pulse. This is suitable when examining pulses in the visible or near infrared wavelength regions, however these mixing schemes are not possible with UV light since phase matching conditions are unable to be met with currently available birefringent crystals. It is possible to use DFG to fully characterize ultrashort UV pulses, however these techniques require an auxiliary pulse that has already been fully characterized, rendering the setup more complicated [53, 54]. Additionally, since this technique requires that two pulses be overlapped temporally, time zero will need to be found again each time the pulse compression is adjusted.

To perform our TPA autocorrelation measurement, the beam to be characterized was split into a strong pump and a weak probe beam and then recombined in the TPA medium. We chose to use a BBO crystal with a thickness of 100μm as our TPA medium for the analysis of the 266.7nm pulses due to its large β value in the wavelength region of 200nm to 330nm [56]. A 0.25 ± 0.01mm thick sapphire cover slip was used for the 200nm autocorrelation measurements due to its greater transmission and β value at this wavelength compared to BBO [56]. Each beam experiences TPA individually upon propagation through the medium, generating a background signal. However, when the two beams are temporally overlapped through the crystal, an additional TPA process occurs with one photon from the pump and one from the probe, as described by equations (3.7.4).

$$\frac{dI_{pump}}{dz} = -\beta I^2{}_{pump} - \beta I_{pump} I_{probe} \quad (3.7.4\text{ a})$$

$$\frac{dI_{probe}}{dz} = -\beta I^2{}_{probe} - \beta I_{pump} I_{probe} \quad (3.7.4\text{ b})$$

Here, z describes the propagation axis through the crystal [56]. The resulting depletion in the probe beam at temporal overlap is recorded, creating an autocorrelation trace.

In order to determine the pulse duration from the autocorrelation trace, we must first assume a Gaussian pulse shape. We can then use the ratio between the FWHM of the autocorrelation trace and that of the pulse, which are both Gaussian functions [40, 58]. For this pulse shape, the FWHM of the autocorrelation trace is given by

$$FWHM_{AC} = 2\sqrt{2\ln 2}\sigma \quad (3.7.5)$$

where σ is the width parameter of the Gaussian function and not the TPA cross section of (3.7.2) [40, 56, 58]. The FWHM of the intensity profile of the pulse, or in other words the pulse duration, is given by

$$FWHM_{p} = 2\sqrt{\ln 2}\sigma \quad (3.7.6)$$

Comparing (3.7.5) and (3.7.6), we can see that the autocorrelation width is a factor of $\sqrt{2}$ larger than the pulse width [40, 58]. This deconvolution factor is all that is needed to extract the pulse length from the autocorrelation trace. Figure 3.9 shows the layout of the autocorrelator setup.

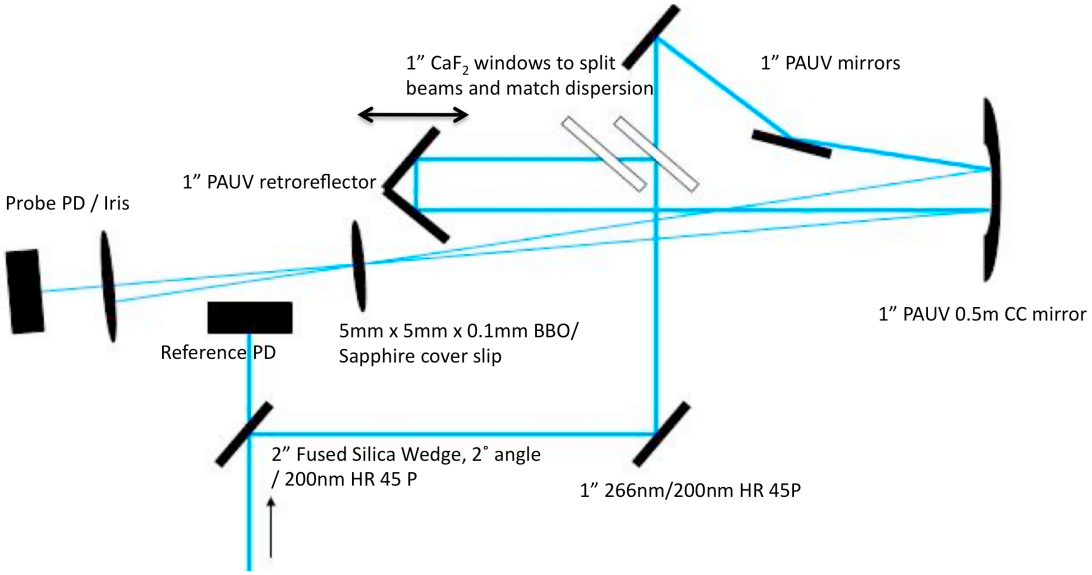

Fig. 3.9 – TPA intensity autocorrelator setup used to measure the pulse durations at 266.7nm and 200nm.

The beam to be characterized was sent into the autocorrelator setup via two steering mirrors. The 266.7nm pulse energy was measured to be 12.3μJ after the prism compressor. As described by Homann *et al*., the power required for TPA measurements only needs to be on the order of a few tens or hundreds of nJ, so a 2" fused silica wedge with a 2° wedge angle was used to send a front face reflection of approximately 95nJ into the autocorrelator via a 1" 266.7nm dichroic high reflector. The post-prism compressor 200nm pulse energy was measured to be approximately 230nJ, a sufficient energy for two 1" 200nm dichroic high reflectors to direct the beam into the autocorrelator.

The beam was aligned to two irises, one at the entrance to the autocorrelator and one just before the photodiode that monitors the probe signal. Upon entering the autocorrelator, the beam was split into a strong pump (transmitted beam) and weak probe (~4% reflection) using a 2mm thick piece of CaF_2. The pump beam encountered two 1" 45° PAUV mirrors that directed it to a 1" PAUV CC focusing mirror with a 0.5m focal length. In order to match the dispersion acquired by the pump beam, the probe was transmitted through an identical

2mm thick piece of CaF_2, as seen in figure 3.9. A pair of 1" 45° PAUV mirrors forming a right angle was used as a makeshift retro-reflector to send the probe beam to the focusing mirror. They were mounted on a motorized stage with a hand-adjustable micrometer screw to optimize the temporal overlap of the probe with the pump beam.

It is important to note that a back face reflection of the probe beam was generated upon encountering the fused silica beamsplitter. We chose the front face reflection to act as the monitored probe beam since the back face reflection will have travelled through more glass than the pump beam. The TPA medium was attached to a mount that allows for translation along the z-axis as well as the perpendicular, horizontal axis, and was positioned such that the center is at the focus of the two beams. A 100μm pinhole was inserted into the TPA mount and used to spatially overlap the pump and probe beams. The second iris placed after the pinhole transmits the front face reflection of the probe beam and acted as a beam dump for the pump. A Thorlabs DET 10A photodiode located after the iris monitored the transmitted probe beam and was used to optimize the location of the TPA medium by translating it along the z-axis until the signal is maximized. This occurred at a distance of 30 cm from the focusing mirror.

Once the beams were spatially overlapped through the pinhole, temporal overlap was found using the micrometer translation stage in the probe line. The depletion in the probe beam that occurs at time zero can be seen with an oscilloscope. A transmission change of ≤15% in the probe beam is desired in order to extract accurate pulse durations from the autocorrelation [56].

The sapphire did not come in a circular aperture able to be attached to the TPA medium mount in the same manner as the BBO, so a small piece was cut with a diamond tip

pen and glued over one of the larger holes in the aperture containing the pinhole using Lepage speed set epoxy. When performing the autocorrelation measurements with 200nm pulses, the pinhole was simply translated sideways using the adjustable mount to bring the sapphire into the focus of the pump and probe beams.

The autocorrelation trace was collected in several steps. First, the photodiode signal from the probe pulse was sent to a boxcar integrator, which gates and integrates the signal, improving the signal to noise ratio and outputting a constant voltage proportional to the probe signal. This constant voltage, referred to as the last sample, was then sent to an A-to-D card, which converts it to a digital signal for collection by a computer. A motorized translation stage was then used to incrementally scan through time zero, which was initially found using the manual micrometer adjustment. The motorized stage was controlled by Labview software and communicated with a Newport ESP 300 motion controller connected to the computer with a GPIB cable. As the translation stage scanned through the temporal overlap of the pump and probe beams, the constant voltage output from the boxcar integrator would change in proportion to the probe signal depletion. The voltage readings at each step of the scan were collected with the same Labview software, building up the autocorrelation trace. Each data point in the trace corresponds to the average of 1000 pulses, and the standard deviation of each data point was used to calculate the uncertainties and plot the error bars. Finally, a Gaussian fit to the data and the subsequent deconvolution to determine the pulse duration were performed with the software.

Shot to shot pulse energy fluctuations introduce additional noise to the probe signal. If the fluctuations are of the same magnitude as the signal itself, the collected data can be difficult to discern from the noise. Therefore, a reference photodiode was used, as described by Homann *et al*. [56], to monitor the transmitted beam through either the fused silica wedge

for 266.7nm, or through the dichroic high reflector for 200nm. The reference signal was also converted to a constant voltage output with a boxcar integrator and then sent to the A-to-D card as a second input. Since the energy fluctuations seen by both photodiodes are correlated, dividing the probe signal by the reference signal in real-time with the Labview software greatly improves the signal to noise ratio.

The results of these autocorrelation measurements along with the performance of each nonlinear mixing step and the measured pulse spectra will be presented and discussed in the following chapter.

Chapter 4: Experimental Results and Discussion

4.1 – Efficiencies of the 266.7nm and 200nm SFG Processes

The first step in characterizing the generated UV pulses is to measure their energies, which correspond to the conversion efficiencies of each nonlinear mixing process. Table 4.1 lists the SNLO calculations of the expected output pulse energies and table 4.2 contains the measured pulse energies from the cryogenic amplifier system. The measurements were performed using an Ophir 3A-FS power meter with an accuracy of 3% [59], and the full beam entering the setup had a total energy of 750 ± 20μJ.

Wavelength Generated (nm)	Input Pulse Energy (μJ)	Output Pulse Energy (μJ)
400	390 (800nm)	120
266.7	210 (800nm) + 100 (400nm)	35
200	150 (800nm) + 25 (266.7nm)	1.8

Table 4.1 – Calculated output energies from SNLO assuming a 5mm beam diameter for SHG.

Wavelength Generated (nm)	Input Pulse Energy (μJ)	Output Pulse Energy (μJ)
400	393 ± 10 (800nm)	47 ± 1
266.7	221 ± 7 (800nm) + 47 ± 1 (400nm)	10.4 ± 0.3
200	100 ± 3 (800nm) + 10.4 ± 0.3 (266.7nm)	0.06 ± 0.002

Table 4.2 – Measured pulse energies before and after each nonlinear mixing step from the cryo amplifier.

Based on the initial SNLO calculations, conversion efficiencies of around 30%, 11% and 1% were expected for the 400nm, 266.7nm and 200nm generation steps, respectively. However, the measured pulse energies presented in table 4.2 were significantly lower than expected. This turned out to be the result of a larger beam diameter than anticipated from the output of the cryo amplifier. The SNLO results were obtained using an 800nm beam with a 5mm diameter for SHG, however as seen in table 3.1, the diameter of the 800nm beam entering the SHG crystal was around 8mm. Since nonlinear frequency-mixing processes are intensity dependent, and intensity is defined as power per unit area, a larger spot size results in a lower intensity, and therefore a lower measured pulse energy.

The beam diameters listed in table 3.1 were then used to redo the initial SNLO calculations, which provided the following expected output pulse energies.

Wavelength Generated (nm)	**Input Pulse Energy (μJ)**	**Output Pulse Energy (μJ)**
400	393 (800nm)	39.4
266.7	221 (800nm) + 39.4 (400nm)	4.1
200	100 (800nm) + 4.1 (266.7nm)	0.07

Table 4.3 – Revised SNLO energy calculations using correct beam diameter from the cryo amplifier.

The experimentally observed output pulse energies agree reasonably well with this revised calculation, however the 200nm energy is still lower than expected from the initial SNLO calculations presented in table 4.1. Based on these results, one would be optimistic that changing the first telescope ratio to give an input beam of 4mm or 5mm in diameter would result in the output energies originally expected. Nevertheless, assuming optimal

spatial and temporal overlap, the greatest differences in conversion efficiency should be a result of poor dispersion management in each 800nm beam used for the mixing steps. For example, the grating compressor in the laser amplifier is typically optimized for the most efficient SHG. However, this will result in longer pulses for the other two 800nm beams used for 3rd and 4th harmonic generation. Therefore, even with smaller beam diameters to increase the output energy of each generated pulse, the lack of simultaneous dispersion management will affect the conversion efficiencies in each step.

The beam diameters from the Legend Elite Duo were then measured in the same manner as described in chapter 3, and are listed in table 4.4 for each wavelength.

Wavelength (nm)	**Nonlinear Mixing Stage**	**Beam Diameter (mm)**
800	(SHG)	5.5 ± 0.05
800	(266.7nm SFG)	4.0 ± 0.05
400	(266.7nm SFG)	3.8 ± 0.05
800	(200nm SFG)	2.8 ± 0.05
266.7	(200nm SFG)	2.8 ± 0.05
200	N/A	2.0 ± 0.05

Table 4.4 – Measured beam diameters for each wavelength from the DUO amplifier system.

The pulse energy of each wavelength was then measured and used to redo the SNLO output energy calculations in order to see if the setup was still performing as expected, as

seen with the cryo amplifier output. Tables 4.5 and 4.6 list the expected and measured pulse energies, respectively.

Wavelength Generated (nm)	Input Pulse Energy (μJ)	Output Pulse Energy (μJ)
400	340 (800nm)	95
266.7	221 (800nm) + 39.4 (400nm)	30
200	100 (800nm) + 4.1 (266.7nm)	0.4

Table 4.5 – Calculated output energies from SNLO using beam diameter from the Legend Elite DUO amplifier.

Wavelength Generated (nm)	Input Pulse Energy (μJ)	Output Pulse Energy (μJ)
400	340 ± 10 (800nm)	110 ± 3
266.7	195 ± 6 (800nm) + 110 ± 3 (400nm)	11.0 ± 0.3
200	108 ± 3 (800nm) + 11.0 ± 0.3 (266.7nm)	0.23 ± 0.007

Table 4.6 – Measured pulse energies of each generated wavelength from the DUO amplifier.

These new energy measurements show improved conversion efficiencies compared to those measured using the cryogenic amplifier. SHG was achieved with a conversion efficiency of 32 ± 2%, and the 266.7nm and 200nm beams were generated with conversion efficiencies of 3.6 ± 0.2% and 0.2 ± 0.01%, respectively. The smaller initial 800nm beam radius is responsible for the larger output energies at each step. Furthermore, increasing the ratio of the third telescope from 1.5:1 to 2:1 resulted in improved spatial overlap of the

800nm and 266.7nm beams, and therefore greater energy in the 200nm light. Nonetheless, the 3rd and 4th harmonic energies are again lower than expected, however the conversion efficiencies in each step do agree fairly well with those from the SNLO simulations given the many uncertainties such as the beam spot size, the pulse length at each crystal, the exact crystal length, the efficiencies of the anti-reflective coatings, power head measurement errors, etc.

As with the case of the cryo amplifier, the compression in the DUO amplifier was optimized for SHG, which explains the high conversion efficiency in this step. However, as mentioned above, optimizing the fundamental beam for SHG results in longer 800nm pulses for the 3rd and 4th harmonic steps, which could explain the lower than expected energies. Furthermore, the beamsplitters used in the setup were chosen to divide the 800nm fundamental beam between the SHG and the two SFG steps by specific ratios. These splitting ratios were the basis of the SNLO simulations and helped determine the optimal conversion efficiencies. Experimentally, however, the ratios were slightly different, providing less energy than anticipated to each crystal, as seen in table 4.7.

Mixing Step	**Expected 800nm Energy (μJ)**	**Measured 800nm Energy (μJ)**
SHG (400nm, 52% of 800nm)	380	340 ± 10
SFG (266.7nm, 28% of 800nm)	204	195 ± 6
SFG (200nm, 20% of 800nm)	146	108 + 3

Table 4.7 – Expected and measured energies of the 800nm beams after each beamsplitter, according to the splitting ratios.

Chapter 2 showed that the SHG process scales quadratically with input pump power, while the SFG steps scale linearly with each of the incoming fields. Therefore, less energy going into each mixing step will significantly reduce the output energy.

4.2 – Measured Spectra

The next step in the characterization of the generated UV wavelengths is to measure their spectra. This was done with an Ocean Optics HR 4000 high-resolution spectrometer and the accompanying integrating sphere along with Ocean Optics Inc. Basic Acquisition Software.

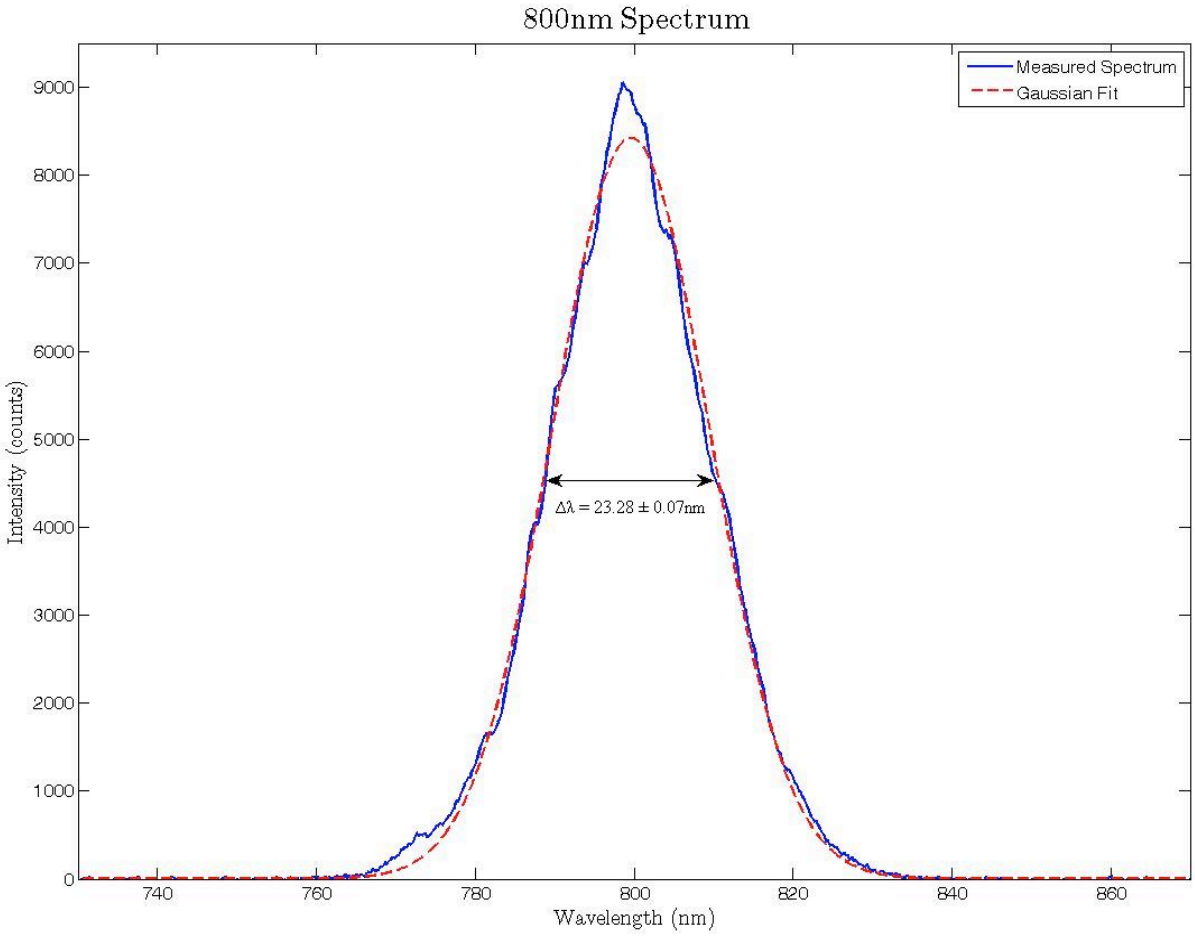

Fig. 4.1 – 800nm spectrum in nm (blue line) with Gaussian fit (red dotted line). The arrow indicates the FWHM of the Gaussian fit.

Using Matlab, the spectral data for each wavelength was fit to a Gaussian function of the form

$$y = ae^{-\left(\frac{x-b}{\sigma}\right)^2} \tag{4.1.1}$$

The FWHM value was extracted from the fit coefficient σ with equation (3.7.6). Figure 4.1 shows the measured 800nm spectrum and its corresponding Gaussian fit, with a calculated FWHM of 23.28 ± 0.07nm indicated by the arrow.

As explained in chapter 2, the spectrum and duration of a laser pulse are fundamentally related through the Fourier transform. Therefore, given the spectral FWHM of each wavelength in the frequency domain, we can calculate the transform limits of each pulse with (2.1.3), using 0.441 for the Gaussian c_B value. These TFL values correspond to the shortest possible pulse lengths supported by the available bandwidth. Therefore, the 800nm spectral width of 23.28 ± 0.07nm corresponds to a TFL pulse length of 40fs. Figures 4.1-4.4 depict the spectra of each pulse in the wavelength scale, and their associated TFL pulse lengths are listed. However, the wavelength scale is not linear in energy, since $\lambda\nu = c$. It is therefore advantageous to plot the spectra in the frequency domain in order to observe how their bandwidth and associated TFL pulse lengths behave after each SFG process. The spectra in the frequency domain will as such be depicted in figures 4.6-4.9.

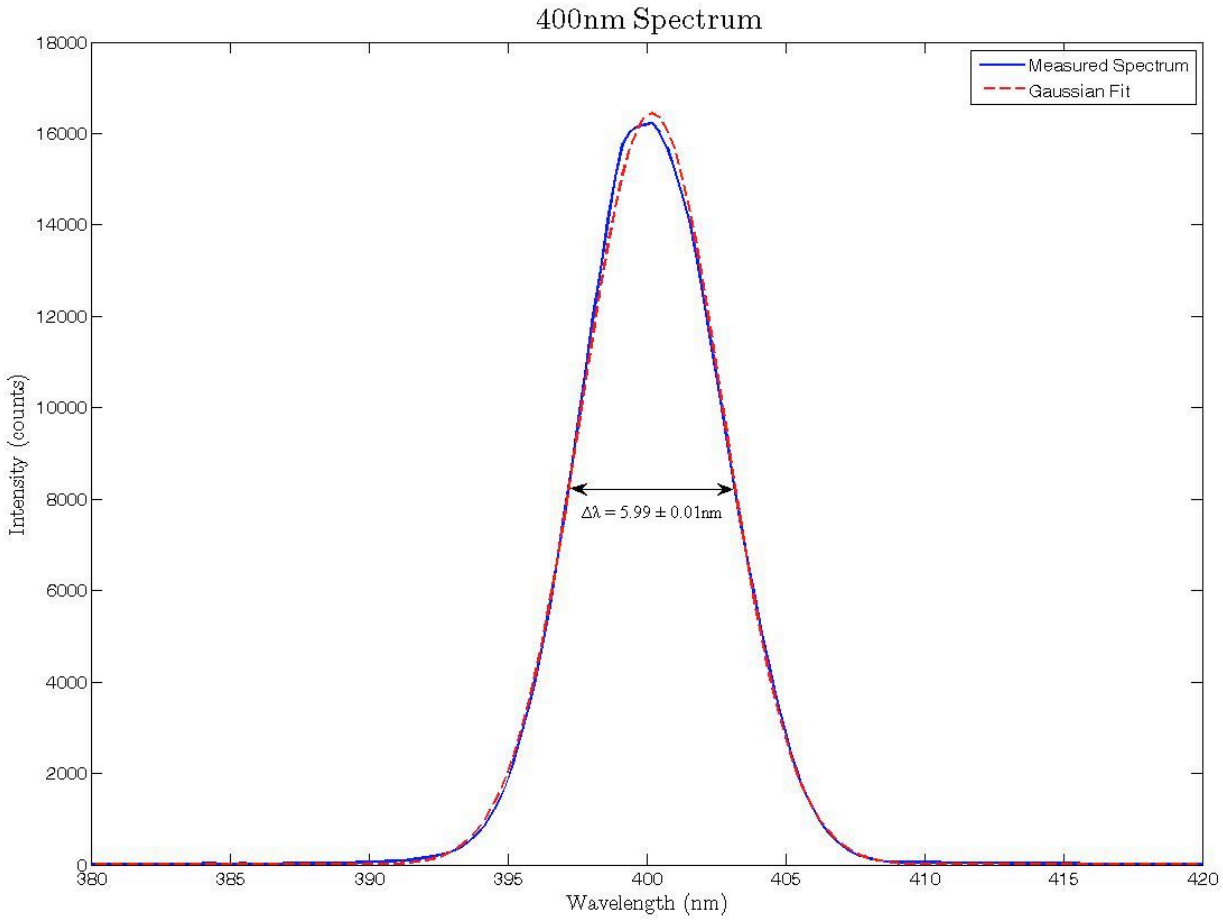

Fig. 4.2 – 400nm spectrum in nm (blue line) with Gaussian fit (red dotted line). The arrow indicates the FWHM of the Gaussian fit.

The 400nm spectrum, shown in figure 4.2, is significantly narrower than the 800nm spectrum, with a FWHM of 5.99 ± 0.01nm corresponding to a TFL pulse length of 39fs. The spectral envelope is also more Gaussian in shape than the 800nm spectrum of figure 4.1. The structure seen in the 800nm spectrum is likely a result of SPM introduced by transmission through the beam splitters before entering the experimental setup. It is possible that this structure, especially in the wings, was smoothed out during the SHG process since it is the most intense portion of the beam that is doubled most efficiently.

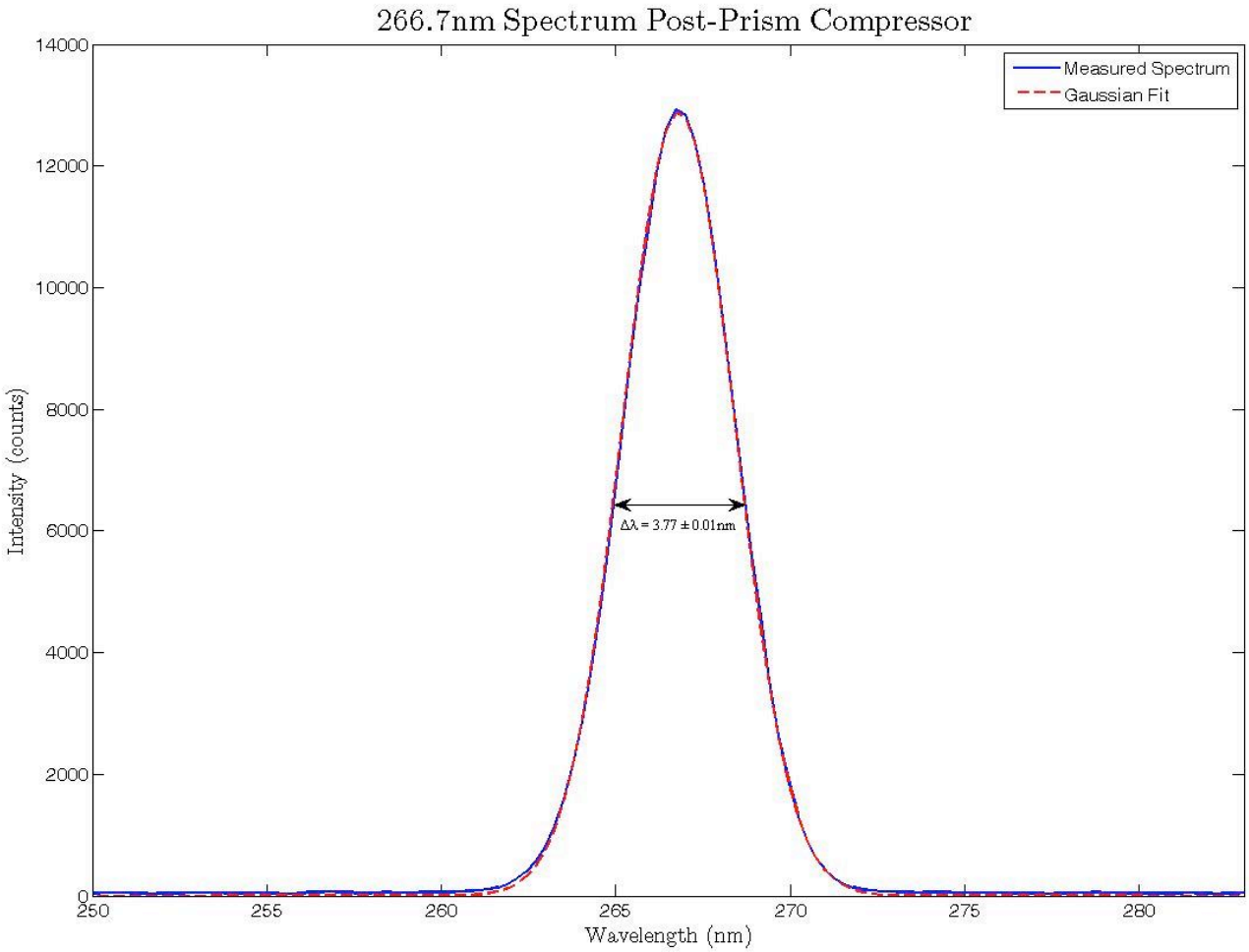

Fig. 4.3 – 266.7nm spectrum in nm (blue line) with Gaussian fit (red dotted line). The arrow indicates the FWHM of the Gaussian fit.

The spectrum of the generated 266.7nm light has a spectral width of 3.77 ± 0.01nm, corresponding to a TFL pulse length of 28fs. The SFG step to 266.7nm produces an almost perfectly Gaussian spectrum, as we would expect based on the improvement between the 800nm and 400nm spectra.

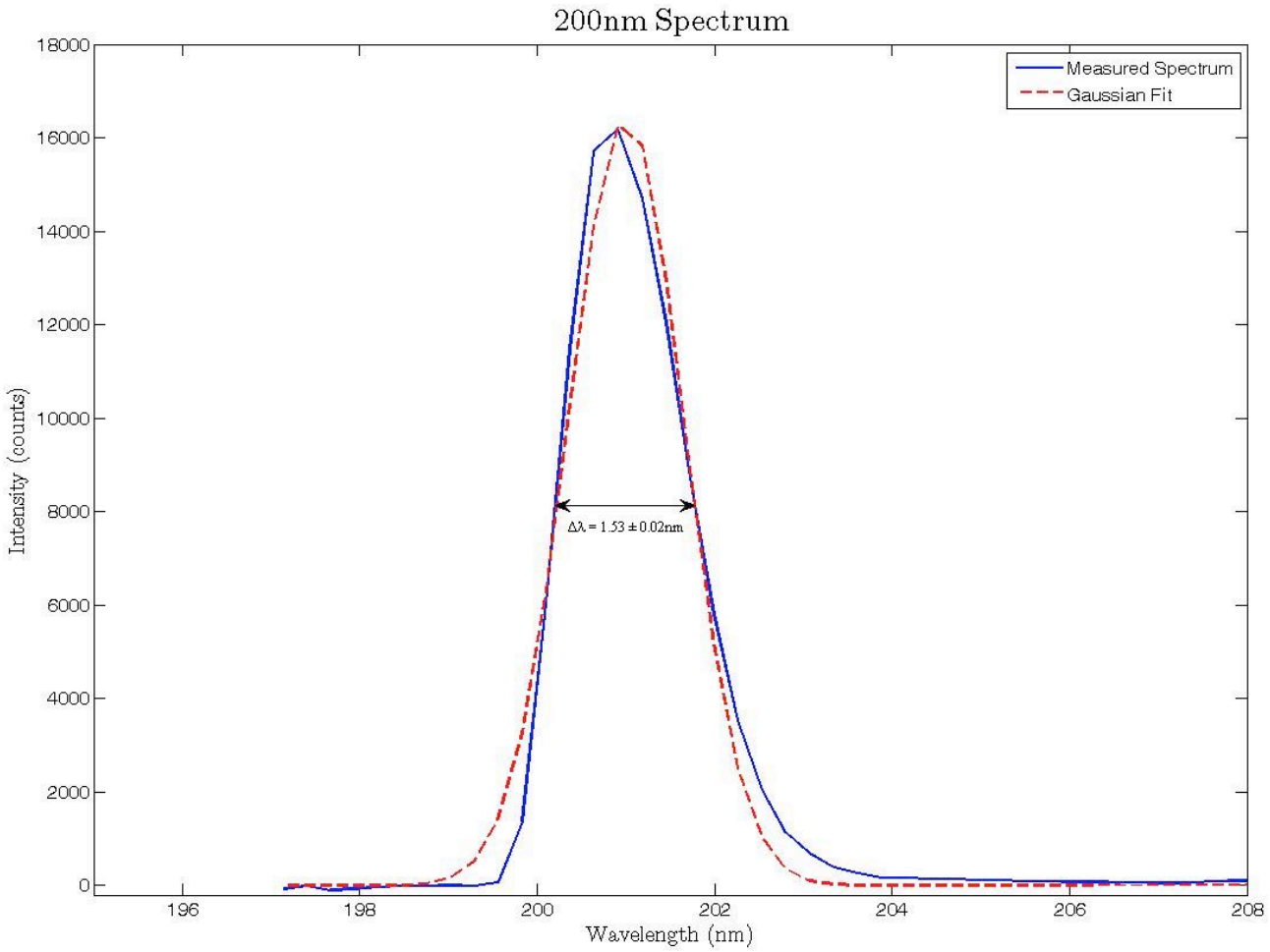

Fig. 4.4 – 200nm spectrum in nm (blue line) with Gaussian fit (red dotted line). The arrow indicates the FWHM of the Gaussian fit.

It is slightly more difficult to accurately measure the spectrum of the 200nm pulses. This wavelength is centered on the leftmost pixel of the CCD detector array for this particular spectrometer, and as a result the spectrum is cut at the low wavelength side of the spectrum and hence does not appear as Gaussian in shape as the 266.7nm spectrum. A different spectrometer optimized to detect wavelengths to either side of 200nm should therefore be used to accurately measure the 4^{th} harmonic spectrum. Due to the cut spectrum, the FWHM of 1.53 ± 0.02nm, corresponding to a TFL pulse length of 38fs, should be considered an upper limit. The 200nm spectrum was measured by sending the beam directly

into the fiber connected to the spectrometer without first passing through the integrating sphere, which is an inefficient way of sending light into the fiber. For low powers, such as the 100's of nJ of 200nm light that we are dealing with, this is the only feasible way to obtain a good spectrum from the Ocean Optics fiber spectrometer.

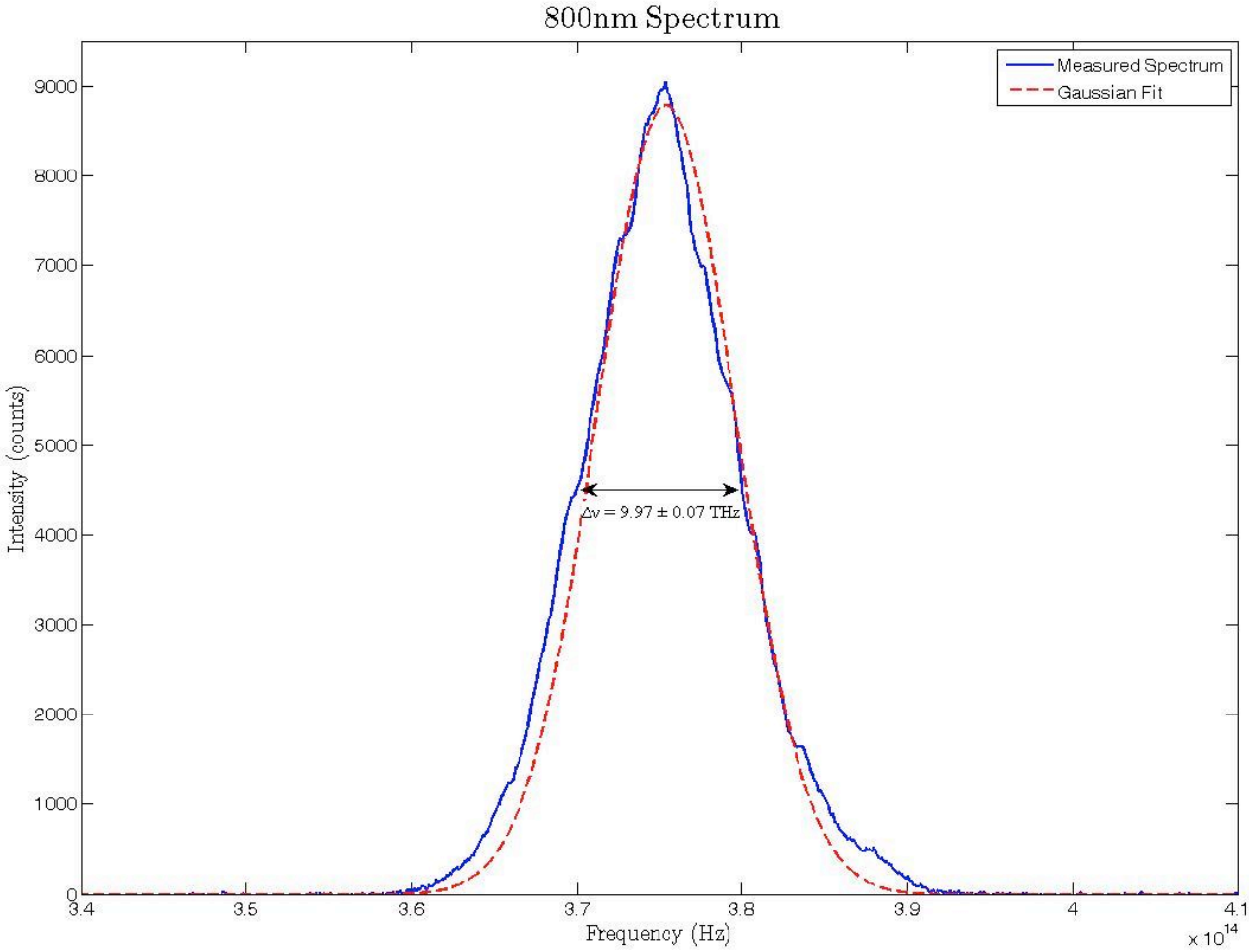

Fig. 4.5 – 800nm spectrum in Hz (blue line) with Gaussian fit (red dotted line). The arrow indicates the FWHM of the Gaussian fit.

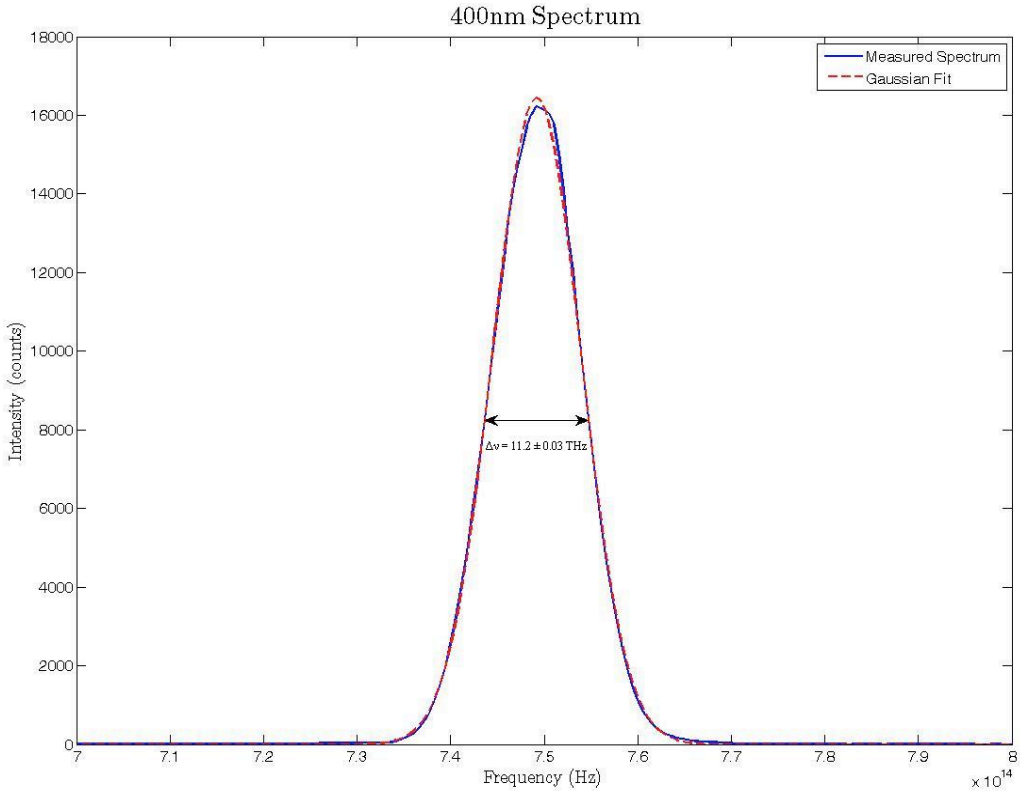

Fig. 4.6 – 400nm spectrum in Hz (blue line) with Gaussian fit (red dotted line). The arrow indicates the FWHM of the Gaussian fit.

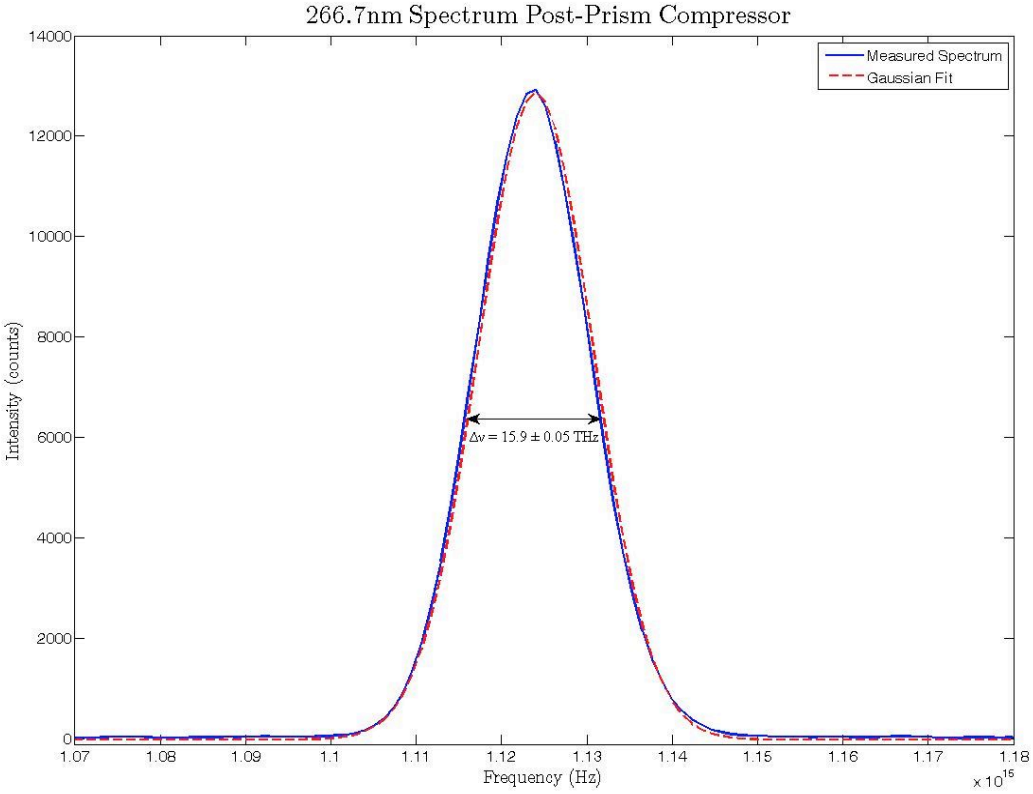

Fig. 4.7 – 266.7nm spectrum in Hz (blue line) with Gaussian fit (red dotted line). The arrow indicates the FWHM of the Gaussian fit.

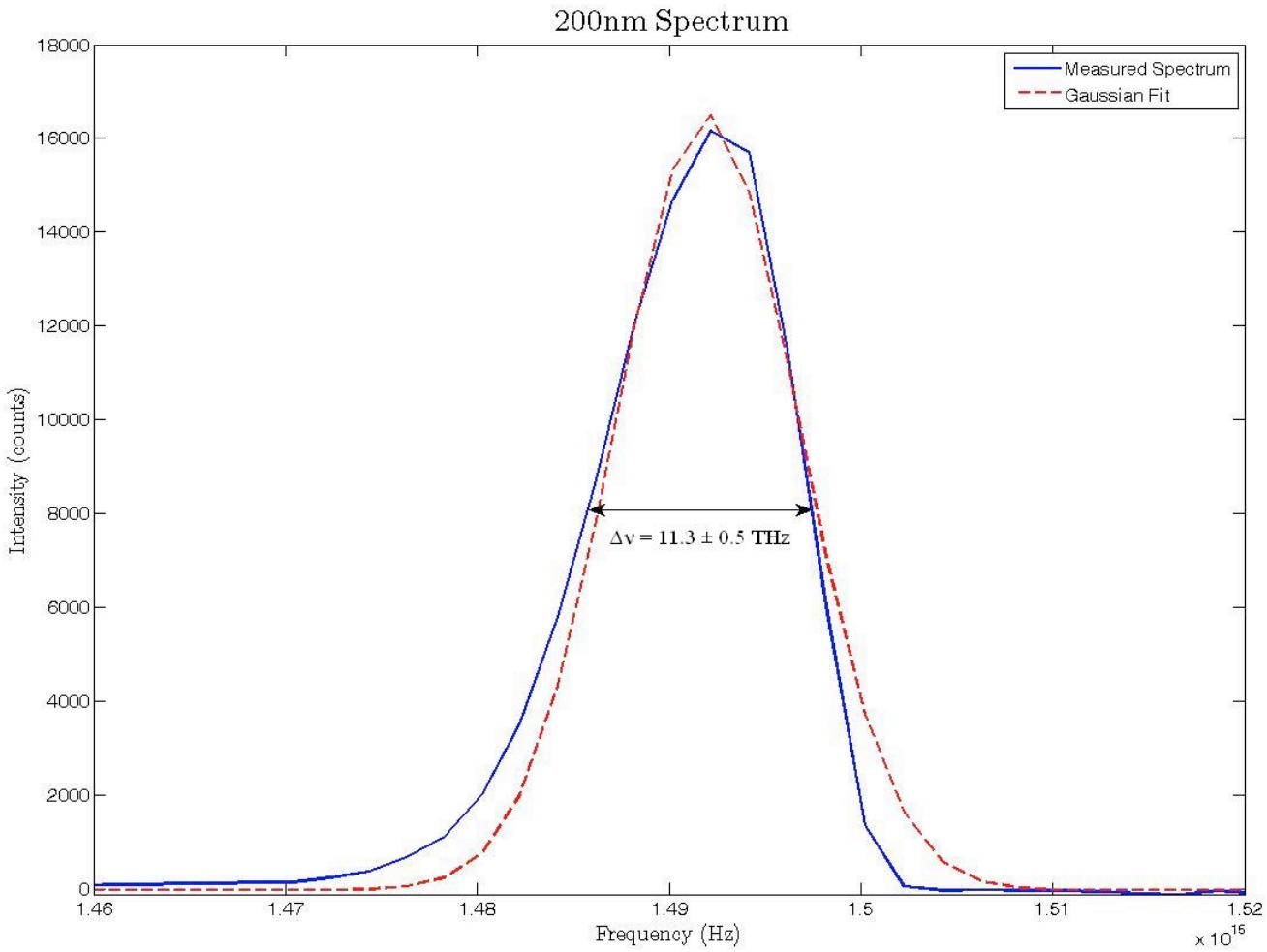

Fig. 4.8 – 200nm spectrum in Hz (blue line) with Gaussian fit (red dotted line). The arrow indicates the FWHM of the Gaussian fit.

Figure 4.5 shows the Gaussian fit to the 800nm spectrum in the frequency domain, and figures 4.6 and 4.7 depict broadening of the spectra with each successive mixing step.

The cutting of the 200nm spectrum observed in figure 4.4 can again be seen at the higher frequency end in figure 4.8. Nevertheless, based on the quality of the spectra of the other wavelengths and their successive broadening, it should be safe to presume that the true 200nm bandwidth would support pulses on the order of 30fs.

With the minimum pulse lengths established from the measured spectra, we know that 35fs pulses should be obtainable for the 3rd and 4th harmonics, and we can now begin their compression to this duration.

4.3 – TPA Intensity Autocorrelation Measurements and Pulse Durations

Using a pulse propagation simulation written in Matlab, we determined the optimal apex-apex separation distance of the prisms in each compressor for a double-pass geometry that would provide maximum compression for the shortest pulses. The program takes as inputs the initial pulse duration, the total amount of glass the pulse will have travelled through (such as recombination optics, beam splitters, a vacuum chamber window, etc.), as well as the amount of glass passed through in the prisms and the apex-apex prism separation distance. The resulting temporal envelope of the output pulse is then plotted against that of the input pulse. The optimal apex-apex distance is found by iteratively varying the prism separation in the program, while keeping all of the other parameters unchanged until the shortest output pulse is generated.

It is often difficult to achieve pulses of as short a duration as the transform limit since the beams pass through dispersive media in the setup such as nonlinear crystals and recombination optics. The durations of the uncompressed 3rd and 4th harmonic pulses were not measured, so initial pulse lengths of 35fs were chosen for these calculations since this duration is supported by the available bandwidth and is short enough for the intended time resolved spectroscopy experiments. The input parameters used for these simulations were the 35fs initial pulse lengths, the measured beam diameters from table 4.4, an apex depth of 10mm through the prism and an estimated travel length of 3mm through fused silica and

3mm of CaF_2 (corresponding to the 0° 200nm dichroic that separates the 3rd and 4th harmonics and the CaF_2 beamsplitter in the TPA autocorrelator). The prism separation required to achieve roughly 36fs pulses at 266.7nm was calculated to be 30cm, and in order to produce 38fs pulses at 200nm, the prisms should be approximately 16cm apart. The results of the simulations are shown in figures 4.9 and 4.10.

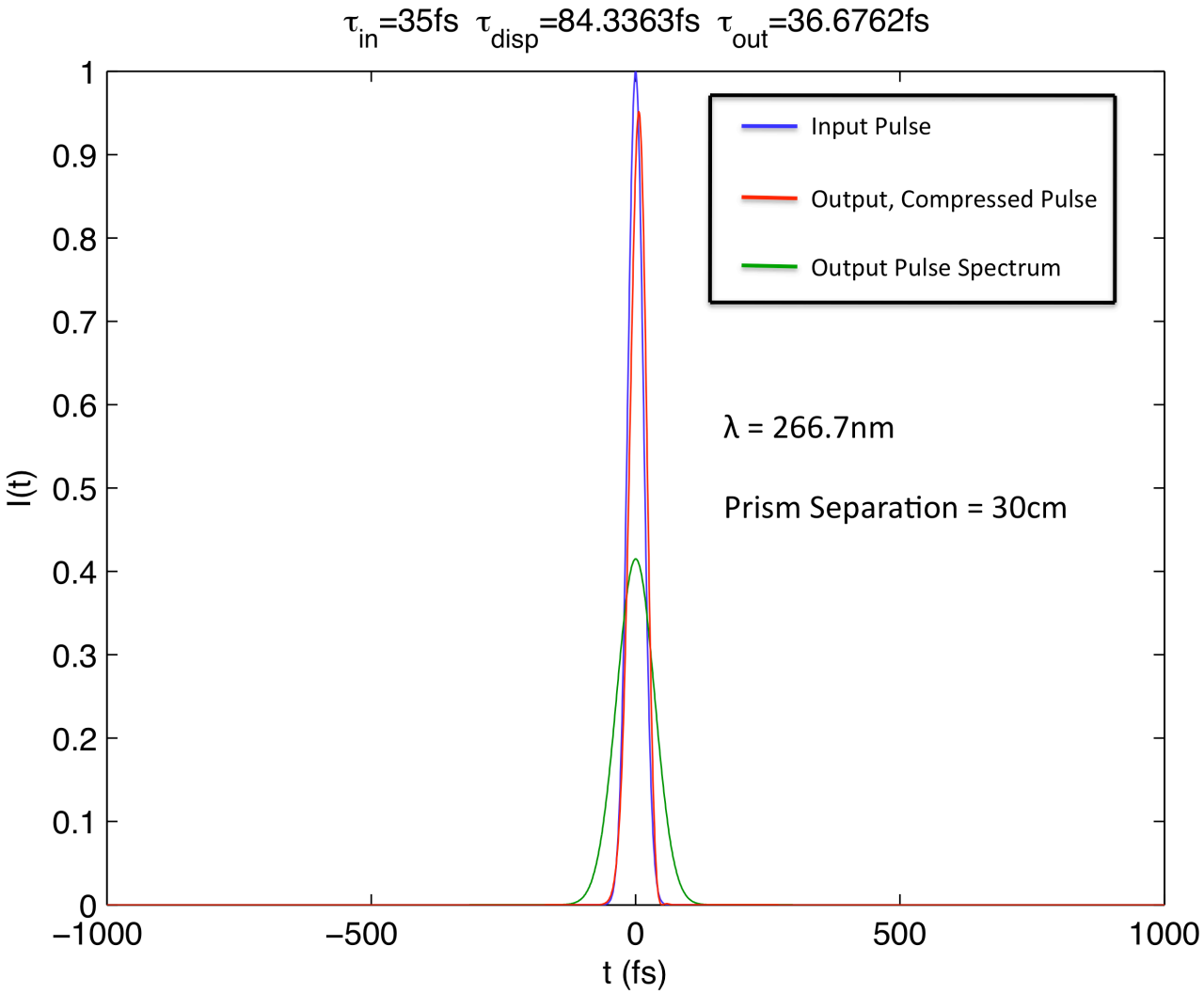

Fig. 4.9 – Prism compressor simulation showing final compressed 266.7nm pulse (red) resulting from a 20cm prism separation distance.

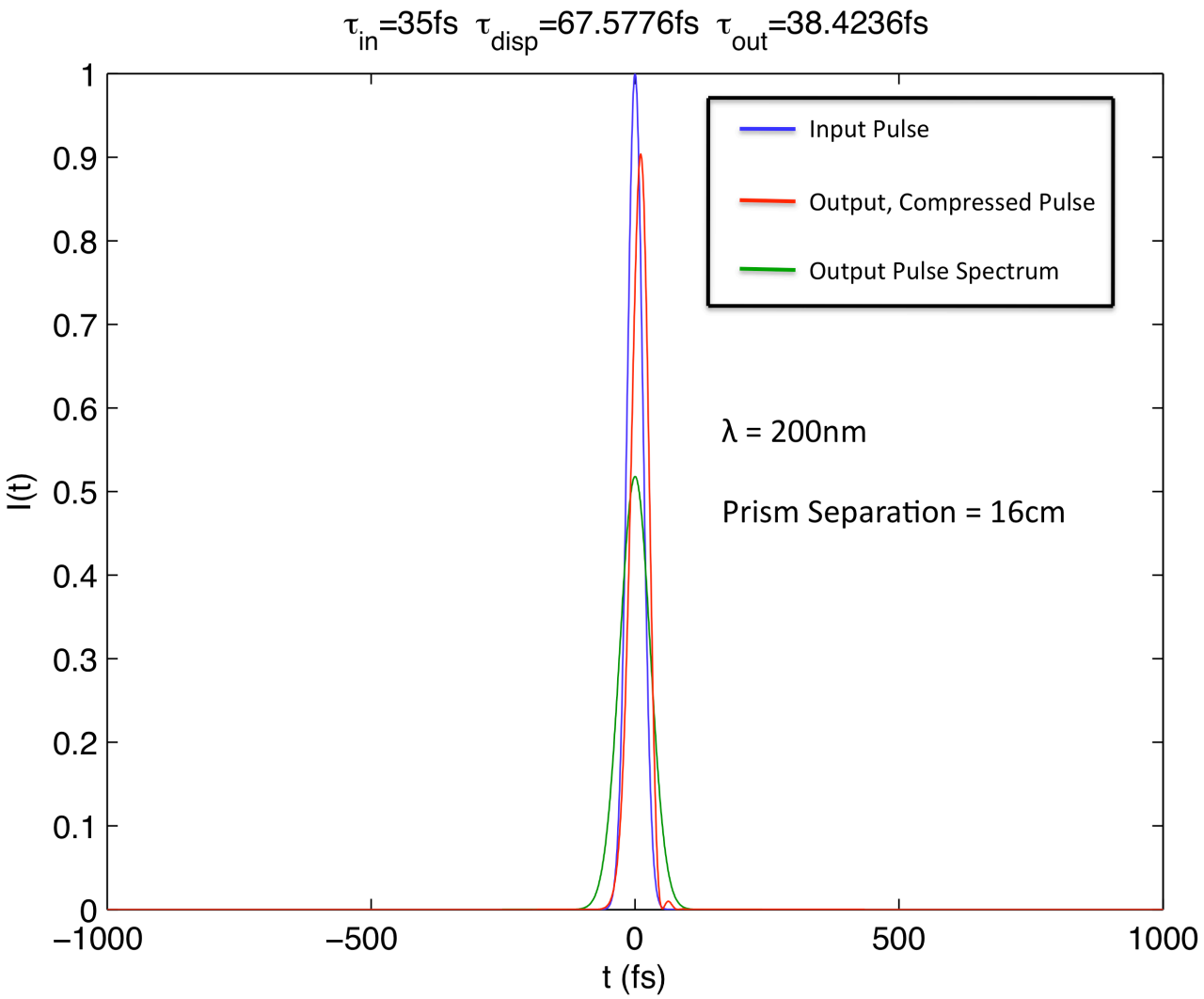

Fig. 4.10 - Prism compressor simulation showing final compressed 200nm pulse (red) resulting from a 16cm prism separation distance.

As mentioned in chapter 3, it is important to use pulse energies of at most a few hundred nJ when performing autocorrelation measurements. Homann *et al*., showed that larger beam intensities result in broader autocorrelation traces, providing misleading results with longer pulse lengths [56]. Furthermore, asymmetries in the autocorrelation trace were observed at higher pulse energies, making it difficult to extract temporal information [56]. Figure 4.11 illustrates this effect, which occurred with 6μJ, 266.7nm pulses.

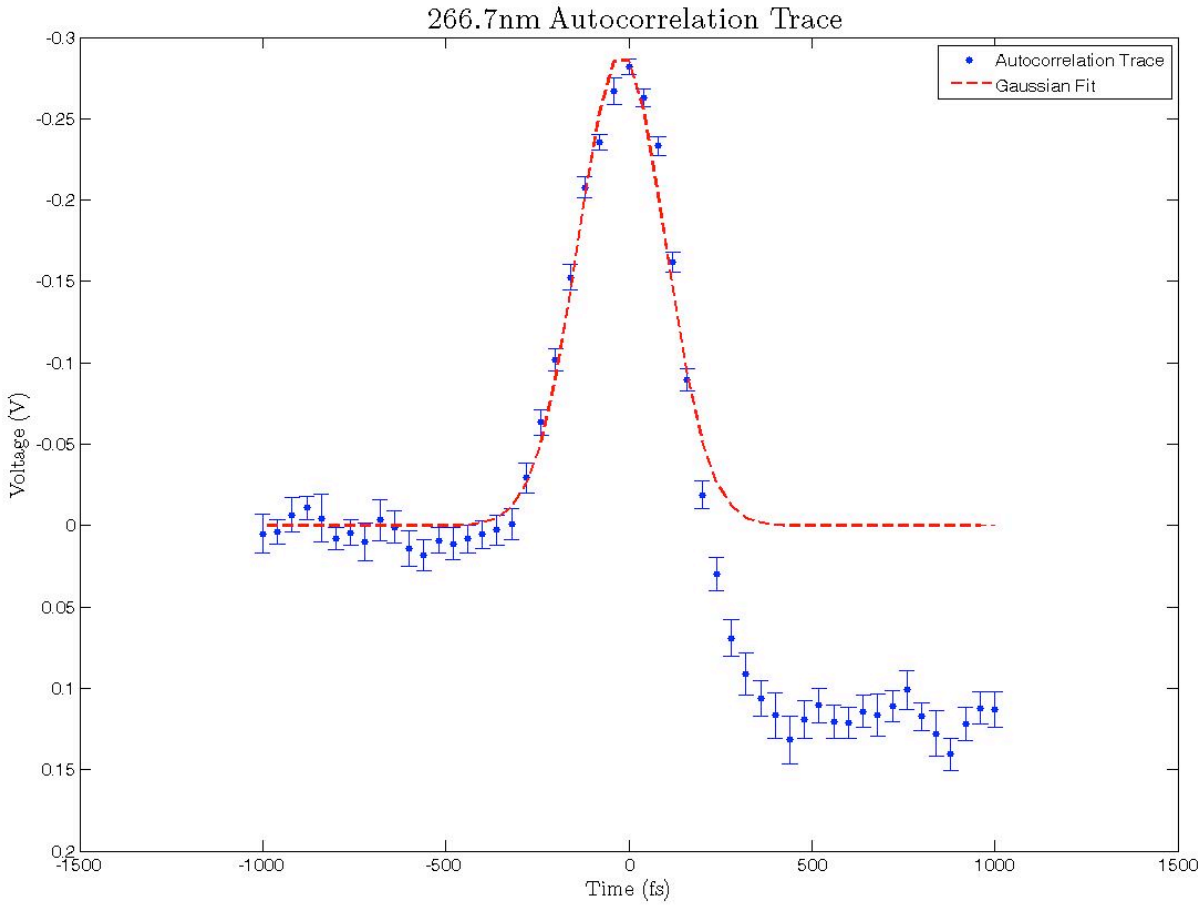

Fig. 4.11 – Asymmetric autocorrelation trace resulting from 6μJ pulses at 266.7nm.

This asymmetry is believed to be a result of long-living free-carrier absorption in the TPA medium [56] and proper fitting of the data with a standard Gaussian function is not possible. The fit shown in figure 4.11 will not provide an accurate value of the pulse duration, so this effect was avoided by using pulse energies of around 95nJ.

The 266.7nm pulses were compressed to a final pulse duration of 36fs at an apex-apex distance of 28.5 cm. Figure 4.12 shows the TPA autocorrelation trace for the fully compressed 266.7nm pulses.

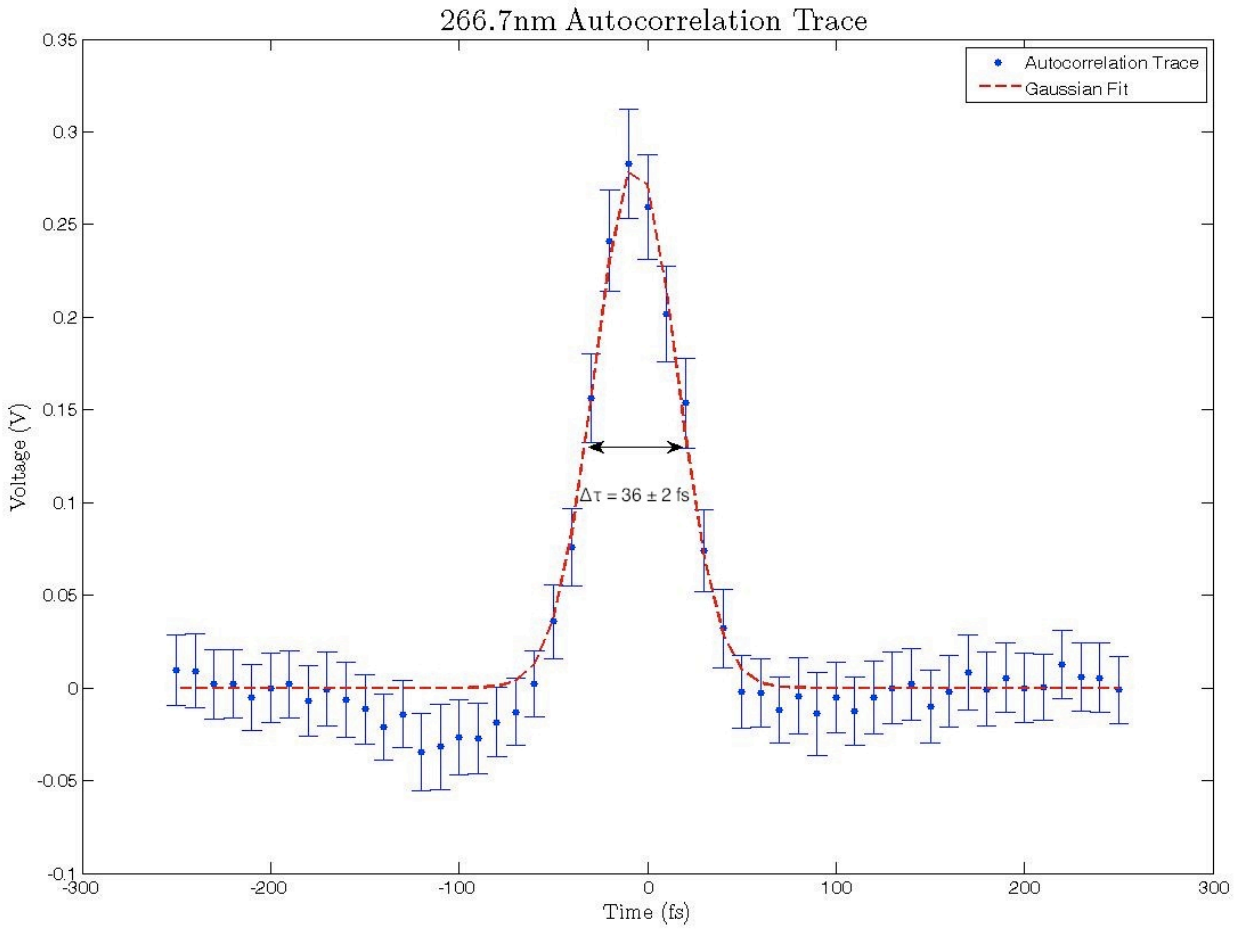

Fig. 4.12 – Intensity autocorrelation trace of fully compressed, 36fs 266.7nm pulse.

It is immediately apparent that the asymmetry seen in figure 4.11 is no longer present at these lower energies, and the fit to the autocorrelation trace is quite good despite some fluctuations in the baseline. It is not likely that the dip in the leading edge of the curve has any insightful physical meaning since it was not reproducible over several successive measurements. One might average the traces over many scans in order to smooth out this particular feature, as well as to acquire a larger data set for the pulse length calculations. However, the main objective of this work was to obtain sufficiently short pulses for use in TRPES experiments, so additional precision in the autocorrelation analysis would be useful from a statistical perspective, but this was not the central focus. Furthermore, the calculated

pulse durations at each prism separation were found to be consistent within experimental uncertainty over many successive measurements. We were therefore confident that the TPA autocorrelator was providing accurate values of the pulse durations, and so the autocorrelation trace most clearly representing the 3rd harmonic pulse duration was chosen for figure 4.12. The shortest pulses were found by iteratively adjusting the apex-apex separation between 28-30 cm, and this pulse length agrees well with the results shown in figure 4.9.

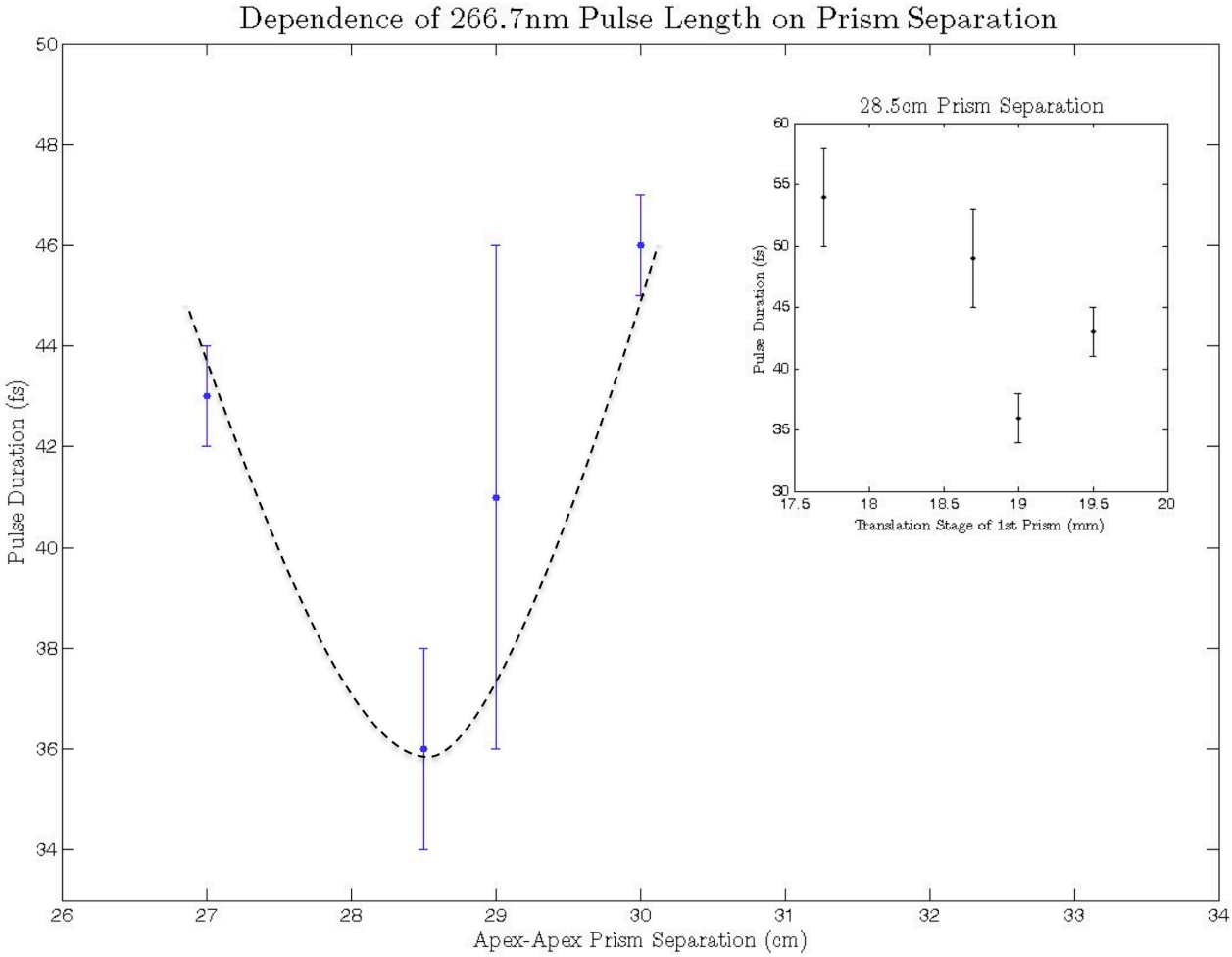

Fig. 4.13 – 266.7nm pulse durations at various prism separations (main plot in blue). The black dotted curve illustrates the general variation in pulse duration about the optimal prism separation. The inset, in black, shows the change in pulse duration with varying amounts of glass at the optimal 28.5cm prism separation.

At each distance examined, the first prism was moved further into the beam path to test if the measured pulse length increased or decreased. If more glass (positive dispersion) in the beam path resulted in longer pulses, then the apex-apex separation (negative dispersion) needed to increase. Conversely, if more glass resulted in shorter pulses, then the prisms were moved closer together.

Figure 4.13 depicts the variation in the pulse length with prism separation for the 266.7nm pulses, shown with blue points. The error bars were determined from the uncertainties in the fit parameters used to calculate the pulse durations. The black dotted curve illustrates the general variation in pulse length about the optimal prism separation of 28.5 cm. The data is somewhat scattered to either side of the minimum pulse length because each time the prism separation distance was adjusted, it was necessary to re-align the prism compressor. Experimentally, this meant that it was not possible to regain the same previous insertion depth of the beam into the prism, and so a clear spread of data was difficult to obtain. Nonetheless, the pulse length can be seen to increases at prism separations both above and below the apex-apex distance of 28.5 cm. In order to ensure that this distance produces the shortest possible pulses, the effect of positive GVD on pulse length was examined at this prism separation and plotted in the inset of figure 4.13. We can see that as the first prism is translated further into the beam path, the pulse reaches its minimum duration before broadening again as positive GVD continues to increase. This confirms that maximum compression has been achieved.

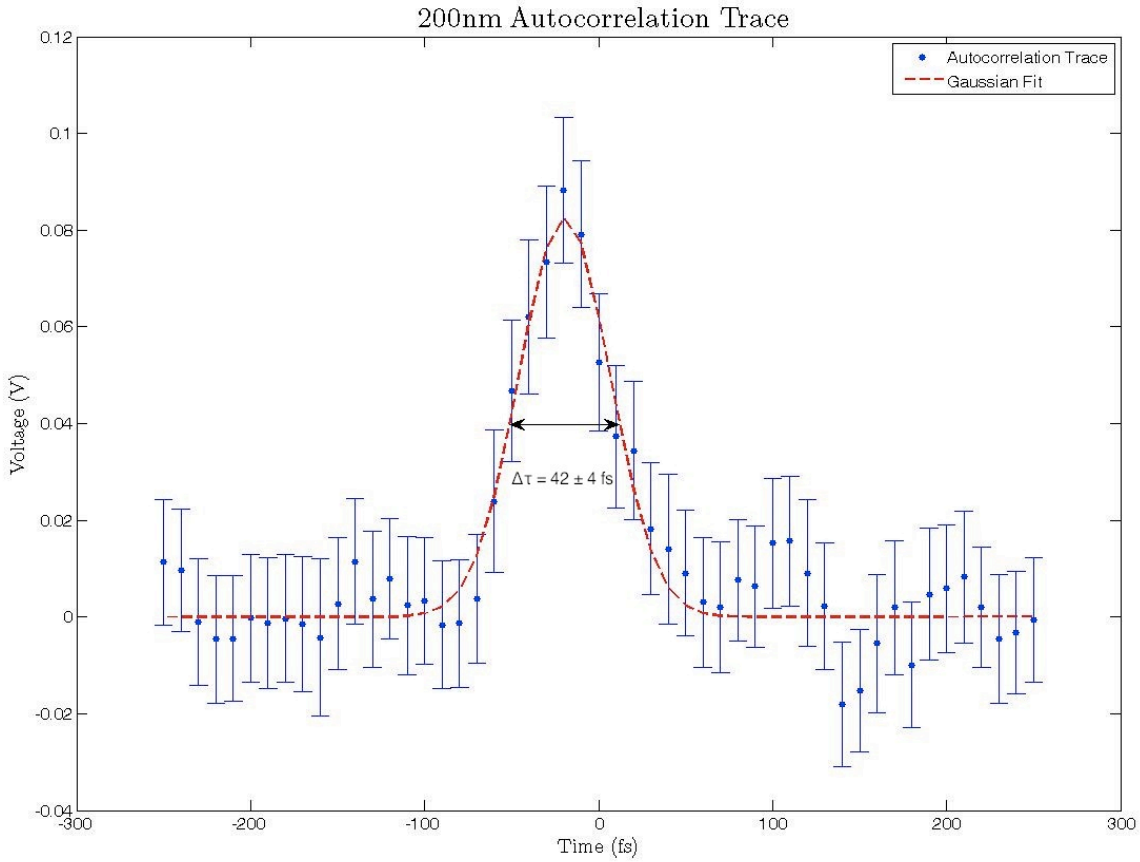

Fig. 4.14 – TPA intensity autocorrelation trace of fully compressed, 42fs 200nm pulse.

The 200nm autocorrelation traces did not exhibit any asymmetries since the pulse energies were on the order of 250 nJ, well below the μJ range. A fully compressed pulse length of 42fs was achieved at a prism separation of 16cm, which agrees with the simulation results within error. Another typical autocorrelation trace, showing a compressed pulse length of 46fs at a prism separation of 15.5 cm, can be seen in figure 4.15.

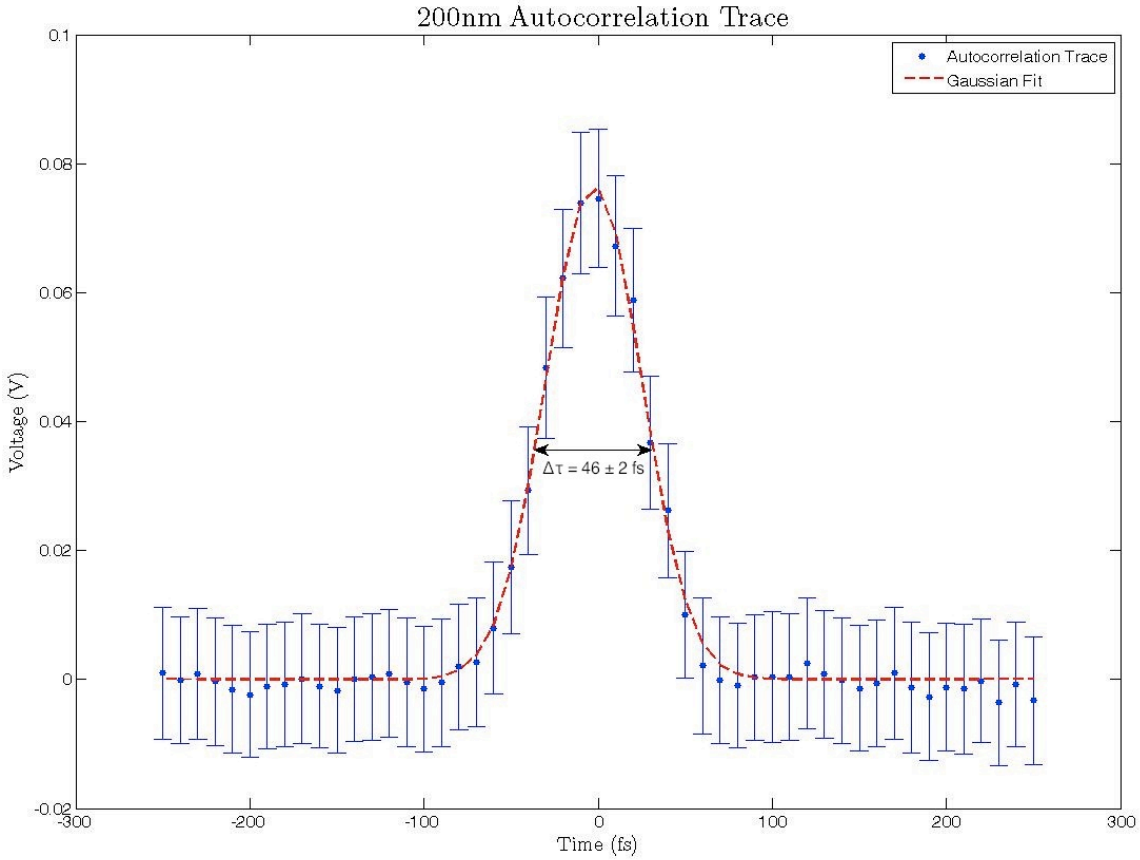

Fig. 4.15 – TPA intensity autocorrelation trace of a 46fs 200nm pulse.

Figures 4.12, 4.14 and 4.15 demonstrate that the TPA intensity autocorrelator is able to successfully measure the 3rd and 4th harmonic pulse lengths. The uncertainty present in the autocorrelation traces is relatively small, considering that a small change is being measured in a strong pulse signal, which contains noise from shot-to-shot energy fluctuations in the laser system. As described in chapter 3, the probe signal is divided by a reference signal in order to improve the signal-to-noise ratio. This normalization is optimized for the peaks of the autocorrelation traces, so it is possible for the outer edges of the traces to be slightly noisier. In addition, if the gated reference signal is not well correlated with the probe pulse signal, the signal-to-noise ratio will be reduced. Nevertheless, the uncertainties in the

pulse lengths were on the order of just a few femtoseconds, which agree with the small fluctuations in pulse length observed from measurement to measurement.

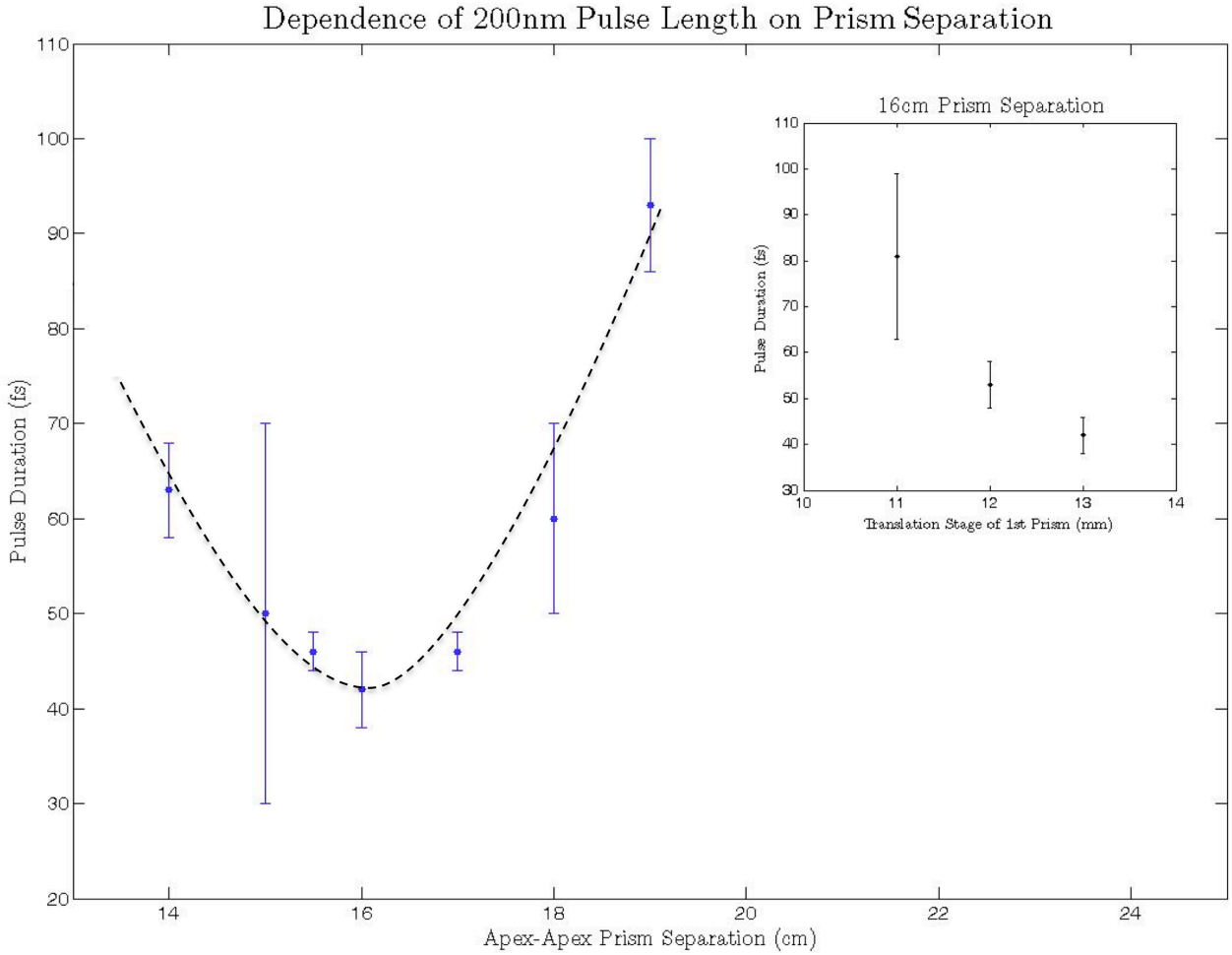

Fig. 4.16 – 200nm pulse durations at various prism separations (main plot in blue). The black dotted curve illustrates the general variation in pulse duration about the optimal prism separation. The inset, in black, shows the change in pulse duration with varying amounts of glass at the optimal 16cm prism separation.

Figure 4.16 presents the 200nm pulse durations at various prism separations. The main plot in blue shows that a clear minimum in the pulse length is present at an apex-apex separation of 16cm. The characteristic increase in pulse duration on either side of the optimal prism separation distance is again highlighted by the dotted black curve. Introducing more glass into the beam path with the first prism resulted in shorter pulses, as shown in the inset of figure 4.16. The shortest pulses were measured at a position of 13mm on the

translation stage, but due to geometrical limitations of the prism compressor setup, we were unable to move the prism any further. Based on the results at 266.7nm, one possible conclusion could be that the 200nm pulse length would increase upon further translation of the prism, verifying the minimum duration of 46fs. The other scenario would be that the pulses in fact become shorter as more glass is introduced.

However, it is far more likely that the inferred 200nm pulse lengths are longer than expected due to broadening of the autocorrelation trace. Homann *et al*. showed a 19% increase in measured autocorrelation widths when the input energy of a 22fs pulse was increased to 200 nJ [56], which is less than the energies used in this work.

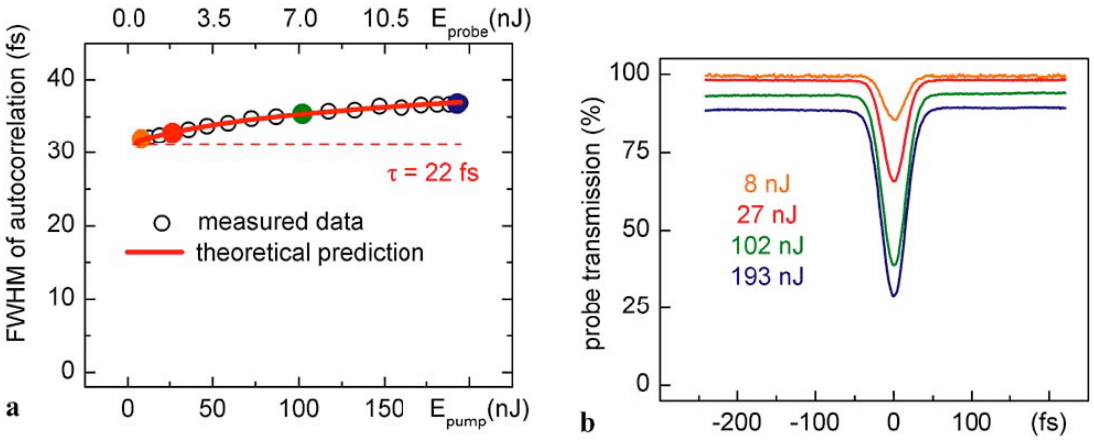

Fig. 4.17 – Increase in FWHM of autocorrelation trace with pulse energy (a), and increase in probe depletion with pulse energy (b) [56].

Another interesting observation was that, while the 200nm pulse energies used for the autocorrelation measurements are greater than the 266.7nm energies, the measured depletion in the 200nm probe beam was often weaker, leading to smaller peaks in the autocorrelation traces. A possible explanation could be that the 200nm beam experienced some absorption in the sapphire window, which was seen as a slight decrease in the individual transmission of

the pump and probe beams. However, as seen in figure 4.17 b), there should be an increase in probe depletion at higher energies, leading us to expect a larger depletion for 200nm than for 266.7nm.

One might argue that since the compressed 200nm pulses are longer than the 266.7nm pulses, their intensities will be lower and therefore less depletion should occur in the probe beam. However, figure 4.17 a) suggests that it is likely that the pulse lengths obtained from the autocorrelation traces are exaggerated, so this explanation for the decreased probe depletion may not be accurate. The 200nm beam should therefore be attenuated using the $\lambda/2$ waveplate in order to send fewer than 100 nJ into the autocorrelator to test this hypothesis. It is also worth noting that the initial prism compressor simulations showed a compressed pulse length of 38fs at a prism separation distance of 16cm. The TFL of 38fs, as determined from the 200nm bandwidth, was determined to be an upper limit, so pulses shorter than 38fs should in principle be possible. Additionally, further efforts should be made to provide a greater translation range for the 1st prism in the 200nm compressor so as to properly locate the minimum pulse duration as a function of positive dispersion.

Chapter 5: Conclusions and Future Work

We have successfully constructed and tested a setup for the generation of the 3rd and 4th harmonics of a Ti:sa CPA fs laser system. Pulse energies of 11μJ and 230nJ at 266.7nm and 200nm, respectively, were generated from the 800nm fundamental pulses with energies of 730μJ. The pulse durations of the 3rd and 4th harmonics were measured with a two-photon-absorption-based autocorrelator to be 36fs and 42fs, respectively, after compression with CaF_2 prism compressors.

The measured output pulse energies from each SFG step differed slightly from the expected pulse energies of 25-30μJ for the 266.7nm pulses and 1μJ for the 200nm light. A spot size of 5mm for the SHG step was used for the initial SNLO calculations, however the beam from the cryogenic amplifier had a diameter of 8mm entering the SHG BBO, reducing the output energy. Revision of the SNLO calculations using the correct spot sizes showed output energies similar to those measured. We thus decided to use the Legend Elite DUO amplifier system in place of the cryogenic amplifier since it provided a spot size of around 5.5mm for the SHG process. The measured energies from the DUO also agreed well with the SNLO calculations using the DUO spot size, providing 3rd and 4th harmonic pulse energies of 11μJ and 0.2-0.3μJ, respectively. It was concluded that the discrepancy between the expected and measured 3rd and 4th harmonic energies was likely due to a lack of dispersion management in their respective 800nm seed pulses, as well as a disparity between the expected and measured performance of the beamsplitters.

The measured spectra had sufficient bandwidth to support 30fs pulses at 266.7nm as well as 200nm, based on the calculated upper limit of the TFL pulse length. In order to verify the TFL pulse length at 200nm, a spectrometer that is able to detect light at the low

wavelength side of the 200nm spectrum should be used. Based on the available bandwidth, we calculated final compressed pulse lengths of 36fs and 38fs at prism separations of 30cm and 16cm for the 3rd and 4th harmonic pulses, respectively. The measured pulse durations after compression at these prism separations were 36fs and 42fs for the 266.7nm and 200nm pulses, respectively, showing nice agreement with the calculations.

The prism compressors were optimized for the scenario where the 3rd and 4th harmonic pulses do not propagate through any further dispersive optics. However, for use with TRPES experiments, one beam must be delayed with respect to the other, and then recombined collinearly into a vacuum chamber for a pump-probe experiment with, for example, a magnetic bottle spectrometer. The pulses will need to enter the vacuum chamber through a window, typically of CaF_2, so the prism compressors must be adjusted accordingly to pre-compensate for this extra dispersion in order to produce the shortest possible pulses inside the chamber.

The time-resolved photoelectron energy spectrum of the Butadiene molecule was previously measured in the lab using a 266.7nm/200nm source, pumped by a Ti:sa amplified CPA system with longer pulses, producing 100fs pulses. It would therefore be an interesting first application of the setup to measure this spectrum using the shorter 3rd and 4th harmonic pulses to see if any new information is present.

Further applications of these short UV pulses could extend to the more robust time-resolved coincidence imaging spectroscopy (CIS) experiments. Typical TRPES experiments are able to disentangle the coupled electronic and vibrational dynamics in molecules, which provides a picture of charge and energy flow in real time [33]. However, information about the intermediate dissociative dynamics is often lost in these experiments due to averaging over the random molecular orientations [33]. Time-resolved CIS experiments overcome this

loss of information by detecting the parent ions and associated photoelectrons in coincidence, yielding fully-correlated 3D energy- and angle-resolved photoelectron-photoion spectra [32, 33]. In previous coincidence experiments with the polyatomic molecule NO_2, Geßner *et. al.* used a pump pulse at 209.6nm and a probe pulse at 279.5nm to study the intermediate state that occurs between excitation and ionization to the NO dimer [33]. Using 160 ± 10 fs pulses, the decay time of the initial state to the intermediate state was measured to be 140 ± 30 fs, and the subsequent decay to the final product state lasted 590 ± 20 fs [33]. It is hoped that future coincidence experiments with NO_2 and other polyatomic molecules using UV pulses on the order of 35fs will yield new information about the dissociative dynamics.

The ability to generate ultrashort UV laser pulses is without question imperative to the realization of TRPES pump-probe experiments, which have proven to be an extremely effective and invaluable tool in the study of molecular dynamics. The more recent development of coincidence imaging techniques has provided even further insight into these fundamental physical processes. The generation and implementation of ever-shorter pulses continues to open up new possibilities not only in the study of ultrafast phenomena, but also in many other industrial and medical applications, pushing our scientific knowledge and abilities toward new heights.

Bibliography

[1] T. H. Maiman, Physical Review Letters **4**, 564-566 (1960).

[2] A. Javan, W. R. Bennett, D. R. Herriott, Physical Review Letters **6**, 106-110 (1961).

[3] W. Kaiser, C. G. B. Garrett, Physical Review Letters **7**, 229-232 (1961).

[4] P. A. Franken, A. E. Hill, C. W. Peters, and G. Weinreich, Physical Review Letters **7**, 118-120 (1961).

[5] M. Bass, P. A. Franken, A. E. Hill, C. W. Peters, and G. Weinreich, Physical Review Letters **8**, 18 (1962).

[6] F. J. McClung and R. W. Hellwarth, Journal of Applied Physics **33**, 828 (1962).

[7] E. Hargrove, R. L. Fork, and M. A. Pollack, Applied Physics Letters **5**, 4-5 (1964).

[8] M. DiDomenico, Jr., J. E. Geusic, H. M Marcos, and R. G. Smith, Applied Physics Letters **8**, 180-183 (1966).

[9] A. J. DeMaria, D. A. Stetser, and H. Heynau, Applied Physics Letters **8**, 174-176 (1966).

[10] J. Kerdiles, Opto-electronics **1**, 193-195 (1969).

[11] M. J. Clobes, A. R., Brienza, Applied Physics Letters **14**, 287 (1969).

[12] H. G. Weber, H. P. Danielmeyer, Physical Review A **2**, 2074-2079 (1970).

[13] R. L. Fork, B. Greene, and C. V. Shank, IEEE Journal of Quantum Electronics **38**, 671-672 (1981).

[14] P. F. Moulton, Journal of the Optical Society of America B **3**, 125 (1986).

[15] W. R. Rapoport and C. P. Khattak, Applied Optics **27**, 2677-84 (1988).

[16] K. Yamakawa, P. H. Chiu, A. Magana, and J. D. Kmetec, IEEE Journal of Quantum Electronics **30**, 2698-2706 (1994).

[17] G. Strickland, D., Mourou, Optics Communications **56**, 219-221 (1985).

[18] H. Schulz, D. von der Linde, SPIE Applications of Ultrashort Laser Pulses in Science and Technology **1268**, 30-40 (1990).

[19] G. Sucha, in *Ultrafast Lasers*, edited by M. E. Fermann, A. Galvanauskas, and G. Sucha, 1st ed. (Marcel Dekker, Inc., New York, NY, 2003), pp. 323-358.

[20] S. Nolte, in *Ultrafast Lasers*, edited by M. E. Fermann, A. Galvanauskas, and G. Sucha, 1st ed. (Marcel Dekker, Inc., New York, NY, 2003), pp. 359-394.

[21] B. N. Chichkov, C. Momma, S. Nolte, F. von Alvensleben, and A. Tünnermann., Applied Physics A **63**, 109-115 (1996).

[22] B. C. Collings, M. L. Mitchell, L. Boivin, and W. H. Knox, Optics & Photonics News 31-35 (2000).

[23] M. Muller and J. Squier, in *Ultrafast Lasers*, edited by M. E. Fermann, A. Galvanauskas, and G. Sucha, 1st ed. (Marcel Dekker, Inc., New York, NY, 2003), pp. 661-697.

[24] A. Zumbusch, G. Holtom, and X. Xie, Physical Review Letters **82**, 4142-4145 (1999).

[25] V. Blanchet, M. Z. Zgierski, T. Seideman, and A. Stolow, Nature **401**, 52-54 (1999).

[26] A. H. Gruebele, M. Zewail, Physics Today 24-33 (1990).

[27] R. W. Schoenlein, L. A. Peteanu, R. A. Mathies, and C. V. Shank, Science (New York, N.Y.) **254**, 412-5 (1991).

[28] I. Fischer, D. M. Villeneuve, M. J. J. Vrakking, and A. Stolow, The Journal of Chemical Physics **102**, 5566 (1995).

[29] P. Kruit and F. H. Read, Journal of Physics E: Scientific Instruments **16**, 313-324 (1983).

[30] H. S. Karlsson, G. Chiaia, and U. O. Karlsson, Review of Scientific Instruments **67**, 3610 (1996).

[31] K. L. Reid, International Reviews in Physical Chemistry **27**, 607-628 (2008).

[32] J. A. Davies, J. E. LeClaire, R. E. Continetti, and C. C. Hayden, The Journal of Chemical Physics **111**, 1-4 (1999).

[33] O. Geßner, A. M. D. Lee, J. P. Shaffer, H. Reisler, S. V. Levchenko, a I. Krylov, J. G. Underwood, H. Shi, A. L. L. East, D. M. Wardlaw, E. T. H. Chrysostom, C. C. Hayden, and A. Stolow, Science (New York, N.Y.) **311**, 219-22 (2006).

[34] W. Radloff, T. Freudenberg, V. Stert, H.-H. Ritze, K. Weyers, and F. Noack, Chemical Physics Letters **258**, 507-512 (1996).

[35] S. Szatmári and F. P. Schäfer, Journal of the Optical Society of America B **6**, 1877 (1989).

[36] J. Ringling, O. Kittelmann, and F. Noack, Optics Letters **17**, 1794-6 (1992).

[37] J. Ringling, O. Kittelmann, F. Noack, G. Korn, and J. A. Squier, Optics Letters **18**, 2035 (1993).

[38] S. X. Dou, D. Josse, R. Hierle, and J. Zyss, Journal of the Optical Society of America B **9**, 687 (1992).

[39] V. Petrov, F. Rotermund, F. Noack, J. Ringling, O. Kittelmann, and R. Komatsu, IEEE Journal of Selected Topics in Quantum Electronics **5**, 1532-1542 (1999).

[40] J. C. Diels and W. Rudolph, *Ultrashort Laser Pulse Phenomena*, 2nd Ed. (Academic Press, New York, 2006).

[41] R. W. Boyd, *Nonlinear Optics*, 3rd Ed. (Academic Press, Amsterdam, 2008).

[42] F. J. Duarte, *Tunable Laser Optics*, 1st Ed. (Academic Press, San Diego, 2003).

[43] A. Smith. SNLO. *AS-Photonics*. http://www.as-photonics.com/SNLO.html (2011).

[44] L. E. Sutton and O. N. Stavroudis, Journal of the Optical Society of America **51**, 901-905 (1961).

[45] G. P. Agrawal, *Nonlinear Fiber Optics*, 3rd ed. (Academic Press, San Diego, California, 2001), pp. 51-55.

[46] R. Paschotta. Beam Radius. *Encyclopedia of Laser Physics and Technology*. http://www.rp-photonics.com/beam_radius.html (2004).

[47] Newport Corporation, Prism Compressor for Ultrashort Laser Pulses, 1-11 (2006).

[48] S. Akturk, X. Gu, M. Kimmel, and R. Trebino, Optics Express **14**, 10101-10108 (2006).

[49] O. E. Martinez, J. P. Gordon, and R. L. Fork, Optical Society of America **1**, 1003-1006 (1984).

[50] R. L. Fork, O. E. Martinez, and J. P. Gordon, Optics Letters **9**, 150-2 (1984).

[51] A. Reuther, A. Laubereau, and D. N. Nikogosyan, Optics Communications **141**, 180-184 (1997).

[52] M. Rasmusson, A. N. Tarnovsky, E. Åkesson, and V. Sundström, Chemical Physics Letters **335**, 201-208 (2001).

[53] C. Iaconis and I. A. Walmsley, Optics Letters **23**, 792-4 (1998).

[54] S. Linden, J. Kuhl, and H. Giessen, Optics Letters **24**, 569-71 (1999).

[55] P. Baum, S. Lochbrunner, and E. Riedle, Optics Letters **29**, 210-2 (2004).

[56] C. Homann, N. Krebs, and E. Riedle, Applied Physics B **104**, 783-791 (2011).

[57] E. W. Van Stryland, M. A. Woodall, H. Vanherzeele, and M. J. Soileau, Optics Letters **10**, 490-2 (1985).

[58] K. L. Sala, G. A. Kenney-Wallace, and G. E. Hall, IEEE Journal of Quantum Electronics **16**, 990-996 (1980).

[59] Laser Thermal Low Power Sensor. *Ophir Photonics*. http://www.ophiropt.com/laser-measurement-instruments/laser-power-energy-meters/products/power-sensors/thermal-low-power (2010).